

Distinguishing between H II regions and planetary nebulae with Hi-GAL, WISE, MIPS GAL, and GLIMPSE*

L. D. Anderson^{1,5}, A. Zavagno¹, M. J. Barlow², P. García-Lario³, and A. Noriega-Crespo⁴

¹ Laboratoire d'Astrophysique de Marseille (UMR 6110 CNRS & Université de Provence), 38 rue F. Joliot-Curie, 13388 Marseille Cedex 13, France.

² Department of Physics and Astronomy, University College London, Gower Street, London WC1E 6BT, UK

³ Herschel Science Centre, European Space Astronomy Centre, ESA, Madrid, Spain

⁴ SPITZER Science Center, California Institute of Technology, Pasadena, CA 91125

⁵ Current Address: Physics Department, West Virginia University, Morgantown, WV 26506, USA.
Loren.Anderson@mail.wvu.edu

Received / Accepted

ABSTRACT

Context. H II regions and planetary nebulae (PNe) both emit at radio and infrared (IR) wavelengths, and angularly small H II regions can be mistaken for PNe. This problem of classification is most severe for H II regions in an early evolutionary stage, those that are extremely distant, or those that are both young and distant. Previous work has shown that H II regions and PNe can be separated based on their infrared colors.

Aims. Using data from the *Herschel* Hi-GAL survey, as well as WISE and the *Spitzer* MIPS GAL and GLIMPSE surveys, we wish to establish characteristic IR colors that can be used to distinguish between H II regions and PNe.

Methods. We perform aperture photometry measurements for a sample of 126 H II regions and 43 PNe at wavelengths from 8.0 μm to 500 μm .

Results. We find that H II regions and PNe have distinct IR colors. The most robust discriminating color criteria are $[F_{12}/F_8] < 0.3$, $[F_{160}/F_{12}] > 1.3$, and $[F_{160}/F_{24}] > 0.8$ (or alternately $[F_{160}/F_{22}] > 0.8$), where the brackets indicate the log of the flux ratio. All three of these criteria are individually satisfied by over 98% of our sample of H II regions and by $\sim 10\%$ of our sample of PNe. Combinations of these colors are more robust in separating the two populations; for example all H II regions and no PNe satisfy $[F_{12}/F_8] < 0.4$ and $[F_{160}/F_{22}] > 0.8$. When applied to objects of unknown classification, these criteria prove useful in separating the two populations. The dispersion in color is relatively small for H II regions; this suggests that any evolution in these colors with time for H II regions must be relatively modest. The spectral energy distributions (SEDs) of H II regions can be separated into “warm” and “cold” components. The “cold” component is well-fit by a grey-body of temperature 25 K. The SEDs of nearly two-thirds of our sample of H II regions peak at 160 μm and one third peak at 70 μm . For PNe, 67% of the SEDs peak at 70 μm , 23% peak at either 22 μm or 24 μm , and 9% (two sources) peak at 160 μm .

Key words. stars: formation - ISM: dust - ISM: H II Regions - ISM: PNe - Infrared: ISM

1. Introduction

Despite their different origins, H II regions and planetary nebulae (PNe) have similar characteristics at infrared (IR) and radio wavelengths¹. The dust associated with H II regions and PNe is responsible for their emission at mid-IR (MIR) to far-IR (FIR) wavelengths. For H II regions this emission is from dust within the H II region itself and from the photodissociation region (PDR), which is the interface between the ionized gas and the interstellar medium (see recent results from, e.g. Deharveng et al. 2010; Anderson et al. 2010; Rodón et al. 2010; Anderson 2011). The IR emission from the PDRs of H II regions comes from neutral material possibly collected during the expansion of

the H II region. For PNe, the IR emission is from the dusty layers of material shed during their creation.

Recently, there has been extensive work on the IR photometric properties of large samples of PNe. PNe have been studied using the IRAC instrument (Fazio et al. 2004) on *Spitzer* by Hora et al. (2004); Cohen et al. (2007); Kwok et al. (2008); Phillips & Ramos-Larios (2008); Zhang & Kwok (2009); Cohen et al. (2011) and also with the MIPS instrument (Rieke et al. 2004) on *Spitzer* by Chu et al. (2009); Zhang & Kwok (2009); Phillips & Marquez-Lugo (2011). Most pertinent for the present study are the results of Cohen et al. (2007, 2011), who showed that PNe should be well-separated from both ultra-compact (UC) H II regions and also more evolved H II regions in IRAC MIR color-color diagrams. These results, however, were based on simulated H II region colors and it remains to be seen if they can be replicated in real measurements.

H II regions and PNe also emit at radio wavelengths. In both cases, the central star(s) produce ultra-violet radiation that ionizes the surrounding medium. This ion-

* *Herschel* is an ESA space observatory with science instruments provided by European-led Principal Investigator consortia and with important participation from NASA.

¹ Technically PNe and H II regions are both “H II regions” in that they contain ionized plasma. Throughout we exclusively refer to “H II regions” as the ionized zones surrounding massive stars, and their associated dust and gas.

ized gas emits radio continuum radiation via thermal Bremsstrahlung (free-free). The radio continuum emission from H II regions is extremely bright; it has been known for some time that most bright continuum sources in the Galactic plane are H II regions. For example, 75% of the bright radio continuum sources in Westerhout (1958) are H II regions and none are PNe. While not as bright, the radio continuum emission from PNe has also been detected for numerous objects (Milne & Aller 1975; Zijlstra et al. 1989; Aaquist & Kwok 1990; Condon & Kaplan 1998). The stars powering H II regions emit considerably more ionizing flux than those powering PNe, and therefore the radio emission from H II regions can be detected at larger distances.

Numerous authors have used data from the IRAS point source catalog to establish criteria for identifying H II regions and PNe. Wood & Churchwell (1989) found that UC H II regions, which are generally young and small in angular size, have characteristic colors of $[F_{25}/F_{12}] \geq 0.57$ and $[F_{60}/F_{12}] \geq 1.30$, where F_λ is the IRAS flux at wavelength λ and the brackets indicate a base ten logarithm. Hughes & MacLeod (1989) found that H II regions have characteristic colors $[F_{25}/F_{12}] \geq 0.4$ and $[F_{60}/F_{12}] \geq 0.25$ while PNe have $[F_{25}/F_{12}] \geq 0.4$ and $[F_{60}/F_{12}] \leq 0.25$. Using different IRAS flux bands, Pottasch et al. (1988) found PNe generally have colors $[F_{25}/F_{12}] \geq 0.46$ and $[F_{60}/F_{25}] \leq 0.52$. These studies demonstrate the power of FIR criteria for locating and discriminating between H II regions and PNe.

Candidate H II regions and PNe can in many cases be distinguished based on visual inspection of their IR emission (e.g. Cohen et al. 2007, 2011). H II regions tend to have more extended emission than PNe, and they show less symmetry. The central stars of PNe are frequently detected at near-IR wavelengths, and this has been used in the “Red MSX Survey” (RMS) survey (Urquhart et al. 2008) to distinguish between the two types of object. While a visual inspection of sources is sufficient in many cases, there are two cases in which visual inspection fails: young H II regions that are not yet extended at IR wavelengths, and evolved H II regions at extreme distances from the Sun. In both cases, the resolution of current MIR surveys does not allow one to distinguish between H II regions and PNe. The problem is the most severe in the case of young, distant H II regions. Visual inspection of course also fails for studies of extragalactic H II regions and PNe where the resolution is insufficient.

The recently completed Green Bank Telescope H II Region Discovery Survey (GBT HRDS Bania et al. 2010; Anderson et al. 2011) illustrates the problem of separating H II regions from PNe. The HRDS sources were selected on the basis of spatially coincident radio and MIR emission. While this criterion easily distinguishes thermally emitting sources (e.g. H II regions and PNe) from non-thermally emitting sources (e.g. supernova remnants and active galactic nuclei), it is not sufficient to distinguish between H II regions and PNe. The number of PNe detected in the HRDS is likely low (Bania et al. 2010), although Anderson et al. (2011) mention a number of cases where the source classification is unclear. The HRDS sources are the most distant H II regions yet detected (L. D. Anderson, 2011, in prep.). Their small angular size may prevent the detection of more diffuse emission, making visual classification unreliable.

The goal of the present work is to establish IR criteria that can be used to distinguish between H II

regions and PNe. These criteria can then be applied to samples of objects of unknown classification, which could greatly increase the number of known H II regions and PNe. The *Herschel* Hi-GAL survey (Molinari et al. 2010), together with WISE (Wright et al. 2010), *Spitzer* MIPS GAL (Carey et al. 2009), and *Spitzer* GLIMPSE (Benjamin et al. 2003; Churchwell et al. 2009) allow us to revisit IR criteria for separating the two classes of objects, at much higher resolution and sensitivity compared to IRAS.

2. Data

2.1. *Herschel* Hi-GAL

The on-going Hi-GAL survey uses the PACS (Poglitsch et al. 2010) and SPIRE (Griffin et al. 2010) instruments of the *Herschel Space Observatory* to map the Galactic plane over the zone $+70^\circ \geq l \geq -70^\circ$, $|b| \leq 1^\circ$, and was recently awarded time to map ~ 240 square degrees in the outer Galaxy as well. Hi-GAL contains photometry bands centered at $70 \mu\text{m}$ and $160 \mu\text{m}$ with PACS, and $250 \mu\text{m}$, $350 \mu\text{m}$, and $500 \mu\text{m}$ with SPIRE. The spatial resolutions of these bands are $6.7''$, $11''$, $18''$, $25''$, and $37''$, respectively. The point source sensitivities of Hi-GAL measured in a complex field are 0.5, 4.1, 4.1, 3.2, and 2.5 Jy/beam for the $70 \mu\text{m}$, $160 \mu\text{m}$, $250 \mu\text{m}$, $350 \mu\text{m}$, and $500 \mu\text{m}$ bands while those in a less complex field are 0.06, 0.9, 0.7, 0.7, and 0.8 Jy/beam (Molinari et al. 2010). The FIR coverage of Hi-GAL traces the emission of dust; the $70 \mu\text{m}$ Hi-GAL band is sensitive to warm (~ 100 K) dust while the longer wavelength bands are more sensitive to colder ($\sim 10 - 30$) K dust.

2.2. WISE

The Wide-field Infrared Survey Explorer (*WISE*) mapped the entire sky in four IR bands: $3.4 \mu\text{m}$, $4.6 \mu\text{m}$, $12 \mu\text{m}$, and $22 \mu\text{m}$. The data used here are from the preliminary data release of 14 April 2011, which cover $\sim 57\%$ of the sky. Along the Galactic plane, this coverage extends approximately from $60^\circ \geq \ell \geq -70^\circ$ and $240^\circ \geq \ell \geq 120^\circ$. The spatial resolutions in the four bands are $6''.1$, $6''.4$, $6''.5$, and $12''$ and the sensitivities are 0.08 mJy, 0.11 mJy, 1 mJy, and 6 mJy, respectively.

Here we use only the WISE $12 \mu\text{m}$ and $22 \mu\text{m}$ bands. The WISE $12 \mu\text{m}$ band should trace similar dust emission components as that of the IRAC $8.0 \mu\text{m}$ band. The $12 \mu\text{m}$ band, however, is significantly broader than that of the IRAC $8.0 \mu\text{m}$ band; within this broad band are PAH features at $11.2 \mu\text{m}$, $12.7 \mu\text{m}$, and $16.4 \mu\text{m}$ (see Tielens 2008). The PAH features at $7.7 \mu\text{m}$ and $8.6 \mu\text{m}$ also fall within the bandpass although at diminished sensitivity. There are also nebular emission lines that may be strong in evolved PNe. The $22 \mu\text{m}$ band should trace the same dust emission components as the $24 \mu\text{m}$ MIPS GAL band (see below).

The WISE $22 \mu\text{m}$ band saturates for point sources at 12.4 Jy (see WISE explanatory supplement²) which is six times higher than that for MIPS GAL, 2 Jy (Carey et al. 2008). We thus expect the WISE $22 \mu\text{m}$ band to be less affected by problems caused by saturation compared to the

² http://wise2.ipac.caltech.edu/docs/release/prelim/expsup/wise-prelrel_toc.html

MIPSGAL 24 μm band. The WISE 12 μm band saturates for point sources at 0.9 Jy.

The WISE image data have units of DN and we use the DN-to-Jy conversion factors of 2.9045×10^{-6} and 5.2269×10^{-5} for the 12 μm and 22 μm bands, respectively (see WISE explanatory supplement²).

2.3. *Spitzer* MIPS GAL

The *Spitzer* MIPS GAL survey mapped the Galactic plane over $+60^\circ \geq l \geq -60^\circ$, $|b| \leq 1^\circ$ using the MIPS instrument. MIPS GAL used two of the three MIPS photometric bands centered at 24 μm and 70 μm . Here we use only data from the 24 μm band, which has a spatial resolution of $6''$. MIPS GAL saturates at $\sim 1700 \text{ MJy sr}^{-1}$ Carey et al. (2008), and strong saturation is present for many star-forming regions and for some PNe (see §5). Unlike the IRAC bands, the MIPS 24 μm data have minimal correction for extended source fluxes (Cohen 2009) and we apply no such correction when computing fluxes.

For H II regions, the 24 μm emission is detected from two distinct zones: along the PDR and also spatially coincident with the ionized gas. These components contribute roughly equally to the 24 μm flux of H II regions (Deharveng et al. 2010; Anderson 2011). The emission coincident with the ionized gas likely comes from very small grains (VSGs) out of thermal equilibrium. The emission from the PDR is probably a combination of emission from VSGs and from a larger grain population whose temperature is closer to 25 K. For PNe, the emission at 24 μm also likely contains contributions from dust at a range of temperatures, but there may also be nebular emission lines that contribute to the emission in this band.

2.4. *Spitzer* GLIMPSE

The *Spitzer* Galactic Legacy Infrared Mid-Plane Survey Extraordinaire (GLIMPSE) mapped the Galactic plane over the same Galactic zone as MIPS GAL using the IRAC instrument. GLIMPSE contains four MIR bands at 3.6 μm , 4.5 μm , 5.8 μm , and 8.0 μm at resolutions of $\sim 2''$. Here we use only the 8.0 μm band because, relative to the other GLIMPSE bands, this band contains fewer stars and more intense diffuse emission. This makes source fluxes easier to measure and decreases errors in the aperture photometry. In addition to being sensitive to warm dust, the 8.0 μm filter contains polycyclic aromatic hydrocarbon (PAH) emission from PAH features at 7.7 μm and 8.6 μm (see Tielens 2008). PAH molecules fluoresce when excited by far-UV photons and thus emit very strongly in H II regions (see *ISO* spectra in Peeters et al. 2002a,b). PAH emission is moderately strong for C-rich PNe and is weak or absent for O-rich PNe (Volk & Kwok 2003; Bernard-Salas 2006).

Scattering within the focal plane causes an increase in the measured flux of extended sources with the IRAC instrument, an effect that is wavelength dependent. To correct for this effect, we follow the *Spitzer* recommendations³ and apply an aperture correction to the 8.0 μm fluxes, based on the size of the aperture. This correction lowers the measured flux values by a maximum of 35% for apertures $\gtrsim 50''$.

2.5. *IRAS*

The *IRAS* satellite mapped 98% of the sky at 12, 25, 60, and 100 μm . In § 5.2.1 we use reprocessed IRAS data known as IRIS (Miville-Deschênes & Lagache 2005) to compare against WISE 12 μm fluxes. IRIS improves on the original IRAS data by correcting for calibration issues, the zero level, and striping problems. The angular resolution of the IRIS data is $3'8 \pm 0'2$, $3'8 \pm 0'2$, $4'0 \pm 0'2$, and $4'3 \pm 0'2$ for the 12, 25, 60, and 100 μm bands, respectively.

3. Source Samples

We require that all H II regions and PNe fall within the boundaries of all the IR surveys used here. At the time of this writing, the Hi-GAL coverage is the most restrictive. It includes longitude coverage from $346.5^\circ > \ell > 290^\circ$, and $3.5^\circ > b > -4.5^\circ$, in addition to a few other more isolated fields. We restrict our samples to the above stated ranges in the southern Galactic plane and about the Galactic center.

3.1. H II Regions

Our goal in creating the H II region sample is to have H II regions spanning a range of evolutionary stages. We make no attempt to create an H II region sample with angular sizes matching that of the PN sample. While many H II regions could not be confused with PNe due to their large angular sizes, if they were located 20 kpc from the Sun the situation would be less clear. By including H II regions spanning a range of physical sizes, we can account for the two situations where an H II region may be confused with a PN: young compact H II regions in an early evolutionary stage and more evolved H II regions at extreme distances from the Sun.

We compile our sample of H II regions from (a) the HRDS (Anderson et al. 2011), (b) the catalog of H II regions detected in recombination line emission prior to the HRDS described in Anderson et al. (2011) (henceforth identified as the “known” sample), and (c) sources classified as H II regions in the RMS survey. The angular sizes of the HRDS targets are typically $\lesssim 2'$, but many are extremely distant (L. D. Anderson, 2011, in prep.). The regions known prior to the HRDS consist mainly of those sources in the recombination line surveys of Caswell & Haynes (1987) and Lockman (1989) for the Galactic zone here studied, although there are also contributions from Lockman et al. (1996), and Sewilo et al. (2004). The RMS survey contains objects detected as point sources in the MSX survey (Egan et al. 2003), excluding the zone within 10° of the Galactic center. Since they are unresolved by MSX, which has an angular resolution of $18'3$ (Price et al. 2001), the MSX targets are small in angular size. The MSX sources used here that were classified as H II regions by the RMS survey all have detected CO emission (Urquhart et al. 2007b) and radio continuum emission (Urquhart et al. 2007a), which together solidify their classification as H II regions. As with the PNe, we only include H II regions in relatively uncomplicated fields.

Our H II region sample contains 126 sources: 21 from the HRDS, 49 from the known sample, and 56 from the RMS survey. This sample of H II regions contains older, evolved regions in the “known” sample, younger H II regions from the RMS survey (many of which are in the ultra-compact

³ See <http://web.ipac.caltech.edu/staff/jarrett/irac/calibration/index.html>

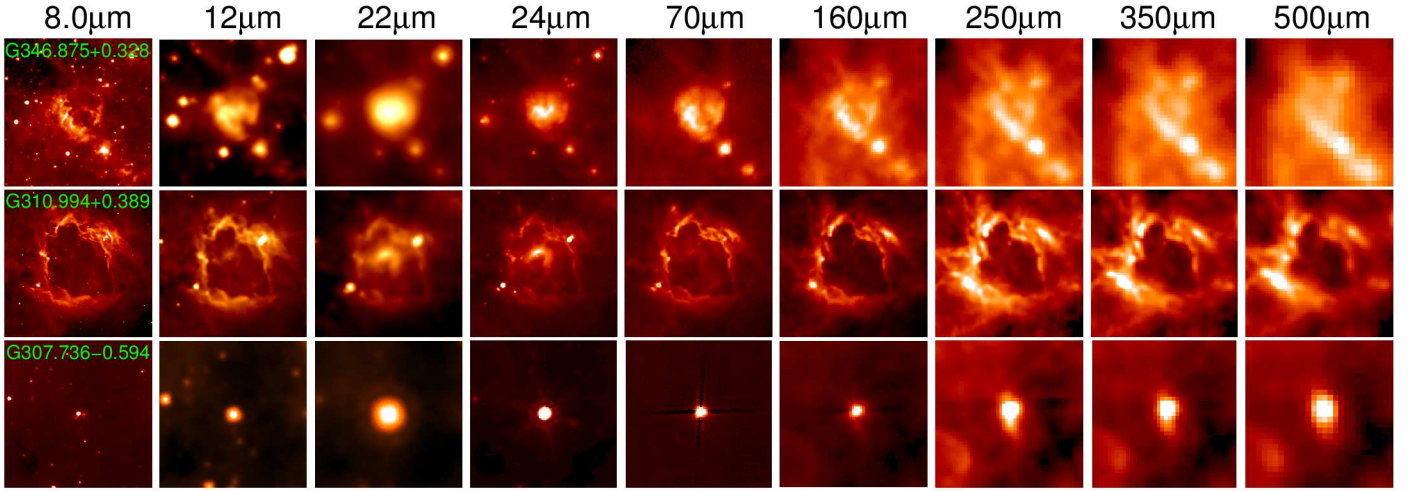


Fig. 1: Infrared images of H II regions from $8.0\,\mu\text{m}$ to $500\,\mu\text{m}$ for three representative sources. Shown are G346.875+0.328, G310.994+0.389, and G307.736−0.594 from top to bottom. The images for G346.875+0.328 and G307.736−0.594 are $5'$ on a side while those of G310.994+0.389 are $12'$ on a side.

phase, as indicated by their compact radio continuum emission measured by Urquhart et al. (2007a)), and the HRDS sources, which likely span a range of evolutionary stages (L.D. Anderson, 2011, in prep.).

Example H II region images are shown in Figure 1, which shows data from $8.0\,\mu\text{m}$ to $500\,\mu\text{m}$. At $8.0\,\mu\text{m}$ and $12\,\mu\text{m}$, if the resolution is sufficient, the H II region PDR appears bright in part because of emission of PAHs. At $24\,\mu\text{m}$ and $70\,\mu\text{m}$, if the resolution is sufficient, the H II region PDRs are detected with a similar morphology as that seen at $8.0\,\mu\text{m}$. There is also, however, IR emission from the region spatially coincident with the ionized gas (see Watson et al. 2008, 2009; Deharveng et al. 2010; Anderson et al. 2011). This emission likely comes from a different dust grain population than the emission in the PDR. It is detected at wavelengths from $12\,\mu\text{m}$ to $70\,\mu\text{m}$ (see G310.994+0.389 in Figure 1). At wavelengths longer than $70\,\mu\text{m}$, the dust emission associated with the H II regions here studied is almost entirely from the colder dust in the PDR. This emission again has a similar morphology as the emission at $8.0\,\mu\text{m}$, although nearby local filaments associated with the H II regions are also sometimes detected. For angularly small sources, the emission from the H II region is frequently found along a filament whose emission at *Herschel* SPIRE wavelengths suggests a cold temperature (for example, the emission from a filament with a dust temperature of 15 K peaks near $200\,\mu\text{m}$ and this filament would emit strongly in the $250\,\mu\text{m}$ SPIRE band). For these sources, their small angular size and location along a cold filament together hint at an early evolutionary stage.

In Figure 1, G346.875+0.328 and G310.994+0.389 would not be confused for PNe due to their extended emission. For G307.736−0.594, however, the situation is less clear from a visual inspection alone.

3.2. Planetary Nebulae

Our goal in creating the PNe sample is to have as many sources as possible, while excluding sources misclassified as PNe. Because we are interested in determining representa-

tive FIR colors, we require that all PNe are detected in at least two of the IR bands considered here.

We compile our sample of PNe from Kohoutek (2001), and the Macquarie-AAO-Strasbourg H α PN Project (MASH) catalogs of more recently discovered PNe (Parker et al. 2006; Miszalski et al. 2008). We also include PNG313.3+00.3 from Cohen et al. (2005). Based on their photometric and spectroscopic observations, the MASH catalogs have a qualitative estimate of whether each source is a “true” PN, or whether it is merely “likely” or “possible”. We include only “true” PNe in our sample and exclude MASH sources classified as “likely” or “possible” PNe. We also exclude PNe in complicated zones of the Galaxy where accurate photometry would be difficult. Following Cohen et al. (2011), we remove objects in Kohoutek (2001) whose classification as PNe is questionable. Our sample includes 43 PNe, 25 from Kohoutek (2001), nine from Parker et al. (2006), eight from Miszalski et al. (2008), and one source from Cohen et al. (2005).

Example PNe images are shown in Figure 2, which shows data from $8.0\,\mu\text{m}$ to $500\,\mu\text{m}$. While many PNe are resolved at $8.0\,\mu\text{m}$, few show extended emission at longer wavelengths. At the longest *Herschel* wavelengths, the emission from PNe is frequently confused with brighter diffuse features.

Our sample of PNe may not be representative of the entire population of PNe in the Galaxy. Our sample is, however, representative of IR-bright PNe that may be confused with H II regions. Many PNe are too faint in the IR to be detected with the survey data used here. For example, Hora et al. (2008) found that of 233 optically identified PNe in the Large Magellanic Cloud, 161 were detected at $24\,\mu\text{m}$ with the MIPS instrument. All sources in our sample are found along the Galactic plane, which may introduce a bias as it will exclude some of the nearest brightest sources that are off the plane.

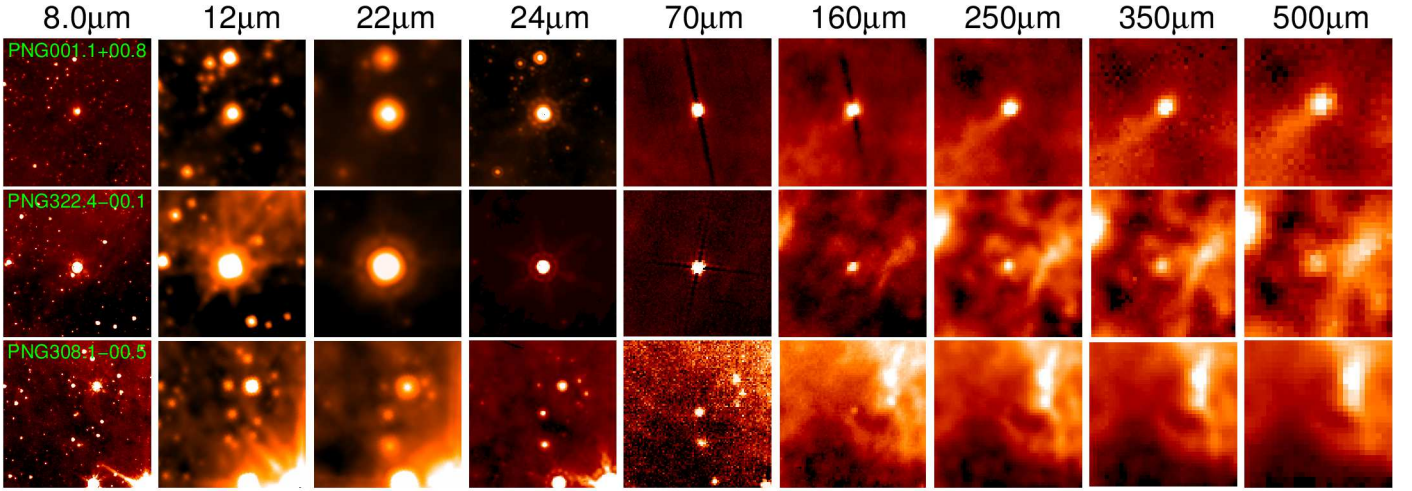


Fig. 2: Infrared images of PNe from $8.0\mu\text{m}$ to $500\mu\text{m}$ for three representative sources. Shown are PNG001.1+00.8, PNG322.4-00.1, and PNG308.1-00.5 from top to bottom. All images are $5'$ on a side. PNG001.1+00.8 and PNG322.4-00.1 are rather bright sources and are detected at all wavelengths, while PNG308.1-00.5 is rather faint and is not detected at wavelengths longer than $160\mu\text{m}$. The increasing confusion with wavelength is evident.

4. Aperture Photometry

We perform aperture photometry for all PNe and H II regions in our sample using the Kang software⁴, version 1.3. This software treats fractional pixels such that if an aperture encloses 30% of the area of a pixel, 30% of the pixel value is included in the aperture flux. Additionally, one can use apertures of arbitrary size and shape and define regions to exclude from the aperture photometry. This flexibility is important for the present analysis in which many regions of interest are in complicated fields, have irregular morphologies, or have nearby contaminating sources of emission.

For the H II regions in our sample, we generally use the same source and background apertures at all wavelengths. When defining apertures we attempt to include all the associated emission at all wavelengths. Most of the H II regions in our sample are bright at IR wavelengths, are relatively unconfused with nearby sources of emission, and have a similar morphology and angular extent at all wavelengths. For nearly all H II regions, a single source aperture for all wavelengths is sufficient to enclose the associated IR flux from the H II region. We make an exception for some angularly small H II regions and for regions in areas whose background emission varies strongly with wavelength. Very small sources sometimes appear within a small cluster of similar sources at $8.0\mu\text{m}$, although at longer wavelengths a single source dominates the emission. An example of this phenomenon is shown in the third row of Figure 1. For such sources we locate the $8.0\mu\text{m}$ source that is spatially coincident with the bright source detected at longer wavelengths. We define a small aperture at $8.0\mu\text{m}$ to isolate the emission from the source responsible for the longer wavelength emission.

We define for each PN separate source and background apertures at each wavelength. Due to their small angular sizes and relatively low IR fluxes, the aperture photometry for the PNe is considerably more sensitive to the aperture size and placement compared to that for H II regions. The choice to define individual apertures at each wavelength

was necessitated in part by the background, which varies strongly with wavelength. An appropriate background at $24\mu\text{m}$ for example may contain large bright diffuse structures at longer wavelengths.

Bright point sources can affect the aperture photometry measurements. For the wavelengths considered here, point source contamination is especially strong from $8.0\mu\text{m}$ to $24\mu\text{m}$, where the contaminants are mostly stellar. We exclude the pixel locations of especially bright point sources by hand from the aperture photometry measurements by defining apertures that avoid such features, but we do not remove point sources from the images. The H II regions in our sample are in general much brighter than the combined flux of any point sources within the aperture at the wavelengths considered here; the removal of point sources would have minimal impact on the derived fluxes. Regions of bright extended emission have a dearth of detected point sources because of the increased Poisson (\sqrt{N}) noise (see Robitaille et al. 2008, their Figure 2). Removing the flux from all detected point sources would therefore assign more flux per unit area to the background region compared to the source aperture, leading to an underestimate of the H II region flux. Due to their small angular size, point source contamination is also not generally a problem for PNe since very few point sources are spatially coincident with the PNe themselves. We make no attempt to exclude all point sources from the background apertures, although we do define apertures to exclude bright point sources. Any flux from low-intensity point sources distributed over the background aperture is likely present in the source aperture as well.

We perform aperture photometry using the relation:

$$S_\nu = S_{\nu,0} - \frac{B_\nu}{N_B} \times N_S, \quad (1)$$

where S_ν is the source flux after the background correction, $S_{\nu,0}$ is the flux within the source aperture (before background correction), B_ν is the flux within the background aperture, N_B is the number of pixels in the background aperture, and N_S is the number of pixels in the source

⁴ <http://www.bu.edu/iar/kang/>

aperture. This treatment subtracts the mean flux within the background aperture from each pixel in the source aperture. The use of the mean flux in the background aperture rather than the median flux should better estimate the contribution from low-intensity point sources.

For all H II regions and PNe we define four background apertures and a single source aperture. We use for the measured flux at a given wavelength the average of the four background-subtracted fluxes found after applying Equation 1 individually to the four source-background pairs. For the uncertainty in flux we use the standard deviation of the four background-subtracted flux measurements.

This method for calculating the flux and uncertainties estimates the true uncertainties associated with our aperture photometry method, which in most cases are dominated by the choice of the background region. In particular, our method accurately estimates errors in fields with strongly varying background emission. In such fields the standard deviation of the pixel values in any given background aperture may be low, but the differences in computed flux between different background apertures may be high.

5. Results

The results of the aperture photometry for the H II regions and PNe are given in Tables 1 and 2, respectively. Both tables contain the source name followed by the source Galactic longitude and latitude and the angular size (radius) of the aperture used at $24\ \mu\text{m}$. For the PNe in Table 2, we list both the Galactic name and the commonly used source identifier. The size column in Table 1 is given in arcmin, while that in Table 2 is given in arcsec. The sizes listed are the “mean radius,” calculated from the area of a circular aperture encompassing the same area as the source aperture. Both tables then list in successive columns the flux in Jy and the uncertainties at $8.0\ \mu\text{m}$, $12\ \mu\text{m}$, $22\ \mu\text{m}$, $24\ \mu\text{m}$, $70\ \mu\text{m}$, $160\ \mu\text{m}$, $250\ \mu\text{m}$, $350\ \mu\text{m}$, and $500\ \mu\text{m}$. If more than 0.1% of the source pixels are saturated at $12\ \mu\text{m}$, $22\ \mu\text{m}$, or $24\ \mu\text{m}$ (see below) these fluxes are marked with the symbol: †. The final column in both tables is the reference.

If 0.1% or more the pixels within a source aperture at a given wavelength are saturated such that they have a value of “NaN,” we exclude this source from all subsequent analyses involving that wavelength. When there is such severe saturation the aperture photometry fluxes are less reliable. Saturation in the MIPS GAL $24\ \mu\text{m}$ data is present for many H II regions and for two PNe in our sample. The WISE data at $12\ \mu\text{m}$ and $22\ \mu\text{m}$ are also saturated for many sources. In Figure 3 we show the ratio of the WISE $22\ \mu\text{m}$ flux to the MIPS GAL $24\ \mu\text{m}$ flux versus the percentage of pixels within the MIPS GAL aperture that are saturated. The average F_{22} to F_{24} ratio for the entire sample of H II regions for which no saturation is detected is 1.05 ± 0.16 (see below); this is shown shaded in Figure 3. The horizontal line at 0.1% separates sources whose $22\ \mu\text{m}$ and $24\ \mu\text{m}$ fluxes are more than 25% different from each other.

Saturation is a problem for many H II regions in the data used here. Forty H II regions have more than 0.1% of their pixels at $24\ \mu\text{m}$ saturated with a value of “NaN”: 26 from the Known sample, 12 from the RMS, and two from the HRDS. Additionally, there are two PNe that satisfy this criterion: PNG358.9–00.7 and PNG359.3–00.9. There

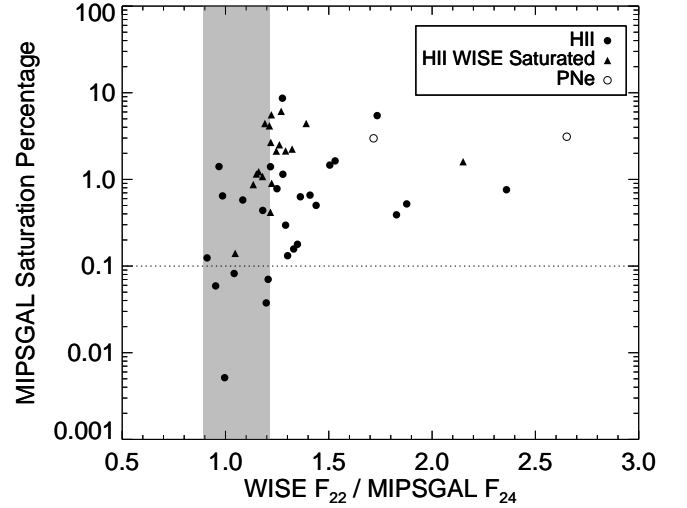


Fig. 3: The ratio of the WISE $22\ \mu\text{m}$ flux to the MIPS GAL $24\ \mu\text{m}$ flux versus the percentage of MIPS GAL pixels that are saturated. H II regions that have some level of saturation in the WISE $22\ \mu\text{m}$ band are shown with open circles and those that do not are shown with filled circles. The two saturated PNe are shown with triangles. The dotted horizontal line shows our cutoff at 0.1% saturated pixels and the grey area shows the standard deviation of the average of the ratio for all non-saturated H II regions. The cutoff at 0.1% separates sources more than one standard deviation from the mean.

is also strong saturation in the WISE data, especially at $12\ \mu\text{m}$. Thirty H II regions in our sample have more than 0.1% of their pixels saturated at $12\ \mu\text{m}$ (25 from the known sample, four from the RMS and one from the HRDS) and 16 satisfy this criterion at $22\ \mu\text{m}$ (15 from the Known sample and one from the RMS). In the WISE bands no PNe in our sample are saturated according to our saturation criterion. PNG359.3–00.9, a PN that shows severe saturation at $24\ \mu\text{m}$, however, has an anomalously low flux at $12\ \mu\text{m}$ compared to its $8.0\ \mu\text{m}$ flux. This indicates that it too may be saturated at $12\ \mu\text{m}$; we exclude it from further analysis involving the $12\ \mu\text{m}$ flux. Some H II regions show mild saturation at $250\ \mu\text{m}$ and $350\ \mu\text{m}$, but none meet the 0.1% cutoff.

5.1. Detection Rates

At each wavelength we visually assess whether each source was detected. Some sources that we count as non-detections may in fact be marginally detected, but they do not allow the high photometric accuracy required for the present analyses. The detection of a source at a particular wavelength is a function of the intrinsic source brightness, the detector and telescope sensitivity, the manner in which the data were taken, and the local background. Whether a source was detected or not at a particular wavelength therefore does not necessarily reflect the intrinsic properties of a source. On average, however, sources detected at a given wavelength are brighter than those that are not detected at that wavelength.

All H II regions in our sample are detected at all wavelengths. All PNe in our sample are detected at $24\ \mu\text{m}$ and $70\ \mu\text{m}$. When creating our PNe sample, however, there were

four PNe only detected in MIPS GAL that otherwise met our criteria; because we require detection in two wavelength bands, we excluded these sources from our PNe sample. This suggests that the $24\mu\text{m}$ MIPS GAL band is the most sensitive of the bands studied here for locating PNe, followed by the Hi-GAL $70\mu\text{m}$ band. Hora et al. (2008) also found that the $24\mu\text{m}$ band was very sensitive to PNe.

All but one PN is detected in the WISE $22\mu\text{m}$ data for a 98% detection rate while three PNe are not detected in the WISE $12\mu\text{m}$ data for a 93% detection rate. At $8.0\mu\text{m}$, 91% of our sample PNe are detected. At wavelengths higher than $70\mu\text{m}$, the detection percentage steadily decreases: 72% of the PNe are detected at $160\mu\text{m}$, 49% at $250\mu\text{m}$, 37% at $350\mu\text{m}$, and 28% at $500\mu\text{m}$. In part because of the decreasing spatial resolution, as the wavelength increases there is considerable confusion with other sources of emission. This contributes to the decreasing detection rates with increasing wavelength, although the intrinsic faintness of PNe at FIR wavelengths is likely a larger factor.

5.2. Fluxes

The H II regions in our sample have significantly higher fluxes compared to the PNe, at all wavelengths. Both samples of objects are composed of relatively bright examples of their classes. The maximum PN flux can be used to set an upper limit that potentially would allow one to separate the two classes.

In Figure 4, we show the two flux distributions for H II regions and PNe in the $70\mu\text{m}$ Hi-GAL data; the distributions for other photometry bands are similar. For our sample of PNe, the maximum fluxes at $8.0\mu\text{m}$, $12\mu\text{m}$, $22\mu\text{m}$, $24\mu\text{m}$, $70\mu\text{m}$, $160\mu\text{m}$, $250\mu\text{m}$, $350\mu\text{m}$, and $500\mu\text{m}$ are 5.3 Jy, 6.2 Jy, 83.2 Jy, 31.4 Jy, 101.6 Jy, 46.0 Jy, 22.3 Jy, 7.7 Jy, and 3.5 Jy, respectively. The maximum $24\mu\text{m}$ value is saturated and the true value should be closer to the $22\mu\text{m}$ value. Objects with fluxes higher than these values are unlikely to be PNe, although in extreme cases a bright PNe may have IR fluxes considerably higher than these limits (e.g. IC 418 or NGC 6302).

5.2.1. A Comparison Between WISE, MIPS, and IRAS

The $22\mu\text{m}$ WISE fluxes are highly correlated with the $24\mu\text{m}$ MIPS GAL fluxes, as shown in Figure 5. This is expected due to their similar wavelengths and bandpass shapes. That the WISE and MIPS GAL fluxes are so highly correlated over five orders of magnitude shows that the fidelity of the WISE preliminary release data is adequate for our analyses here. We find that the WISE $22\mu\text{m}$ band fluxes are on average 1.05 ± 0.16 times the MIPS $24\mu\text{m}$ fluxes for H II regions that are below our saturation threshold. For PNe, the WISE $22\mu\text{m}$ band fluxes are on average 1.01 ± 0.23 times the MIPS $24\mu\text{m}$ fluxes. Many of the sources below the line in Figure 5 are saturated in the $24\mu\text{m}$ band – we have not excluded saturated sources from the figure.

The $12\mu\text{m}$ WISE fluxes are less strongly correlated with IRAS $12\mu\text{m}$ fluxes, as shown in Figure 6. To create Figure 6 we measured the IRAS $12\mu\text{m}$ fluxes for well-isolated H II regions. We used the same method as before, but we defined new apertures to take into account the significantly poorer IRAS resolution. Contrary to Figure 5, Figure 6 shows only sources that are not saturated in the WISE $12\mu\text{m}$ band

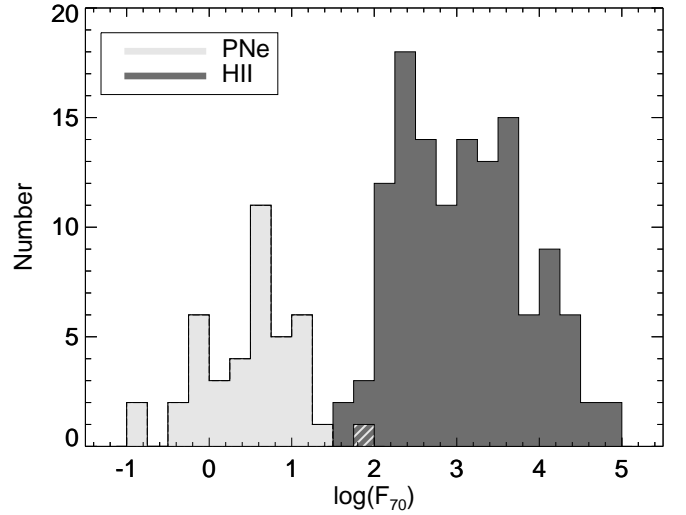


Fig. 4: The distributions of $70\mu\text{m}$ fluxes. The fluxes of H II regions are shown in dark grey while those of PNe are shown in light grey. The hatched box has contributions from both H II regions and PNe. Our sample of H II regions is significantly brighter than our sample of PNe.

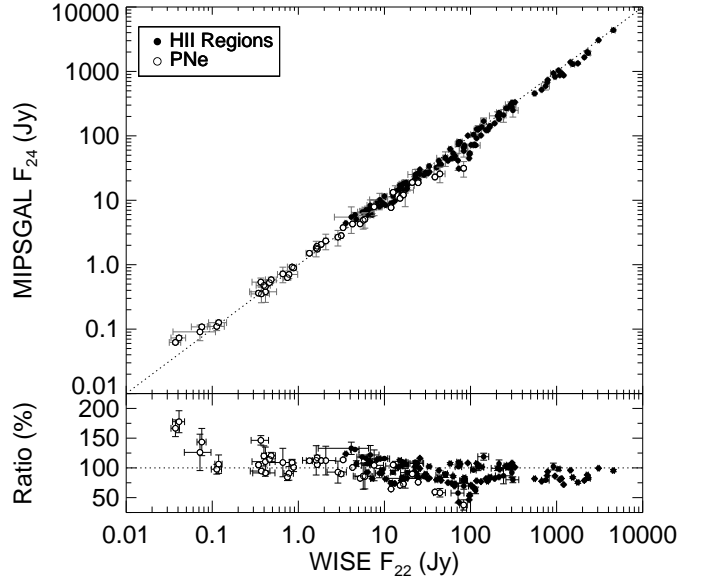


Fig. 5: Correlation between WISE and MIPS GAL. In the top panel we plot the WISE $22\mu\text{m}$ flux versus the MIPS GAL $24\mu\text{m}$ flux; in the bottom panel we show the ratio of the MIPS GAL $24\mu\text{m}$ flux to the WISE $22\mu\text{m}$ flux, as a percentage. The dotted line in both panels shows a one to one relationship. Errors are the 1σ photometric uncertainties. There is a strong correlation between the two fluxes over five orders of magnitude. The sources below the trend line, especially for high values of the flux, indicate MIPS GAL saturation.

according to our saturation criterion. Especially at higher fluxes, we find that the correlation is quite good. Given the larger photometric errors, Figure 6 is less conclusive than Figure 5, although it does also suggest that the photometric quality WISE preliminary release data is high.

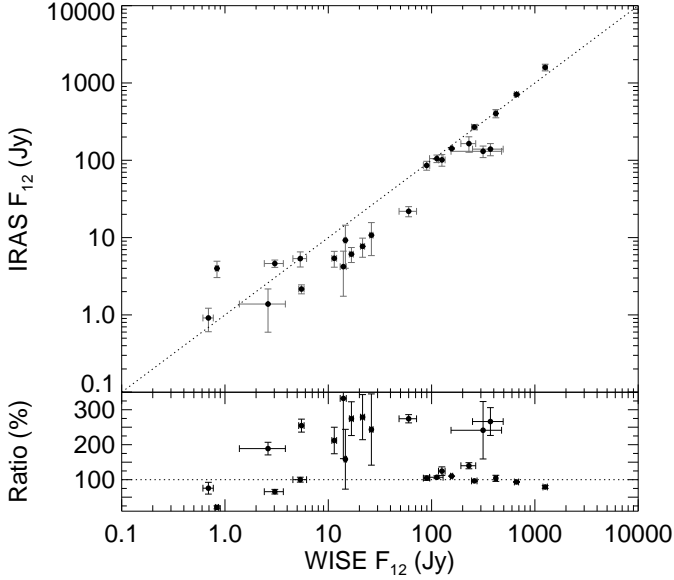


Fig. 6: Correlation between WISE and IRAS. In the top panel we plot the WISE 12 μ m flux versus the IRAS 12 μ m flux; in the bottom panel we show the ratio of the IRAS 12 μ m flux to the WISE 12 μ m flux, as a percentage. The dotted line in both panels shows a one to one relationship. Errors are the 1σ photometric uncertainties. There is a correlation between the two fluxes over four orders of magnitude, although there is significant scatter in the relationship. This scatter is likely due in large part to the difficulty of IRAS photometric measurements. We have included only H II regions that are not saturated in the WISE 12 μ m band.

5.3. Spectral Energy Distributions

Based on the results from IRAS mentioned in the introduction, which showed that H II regions and PNe possess on average different FIR colors, we expect that the shapes of the spectral energy distributions (SEDs) of H II regions and PNe are also different. Spectral observations with the *Infrared Space Observatory* (ISO) have also shown that PNe and H II regions have different mean SEDs (see Cohen et al. 1999; Peeters et al. 2002b); the SEDs of PNe are generally broader than those of H II regions.

The average SEDs normalized to the peak flux for PNe and H II regions are shown in Figure 7. We only include the 12 μ m, 22 μ m, and 24 μ m fluxes in the averages if the sources are not saturated at these wavelengths according to our saturation criterion. For PNe not detected at all wavelengths, we exclude from the averages the contribution from wavelengths where the source was not detected. The IR emission from PNe evolves with time as the dust in the circumstellar shell expands (e.g. García-Lario & Perea Calderón 2003). Even for the same evolutionary state, whether a given PN is oxygen-rich or carbon-rich can affect its IR properties (Volk & Kwok 2003; Bernard-Salas 2006). Thus there is significantly more dispersion in the average PN SED compared to that of the H II regions, as can be seen in the larger error bars in Figure 7.

The difference between the average H II region and PNe SEDs is clear. For H II regions, the SED peak near 100 μ m can be ascribed to “cold” dust, while the MIR emission has contributions from warmer dust and emission lines (largely

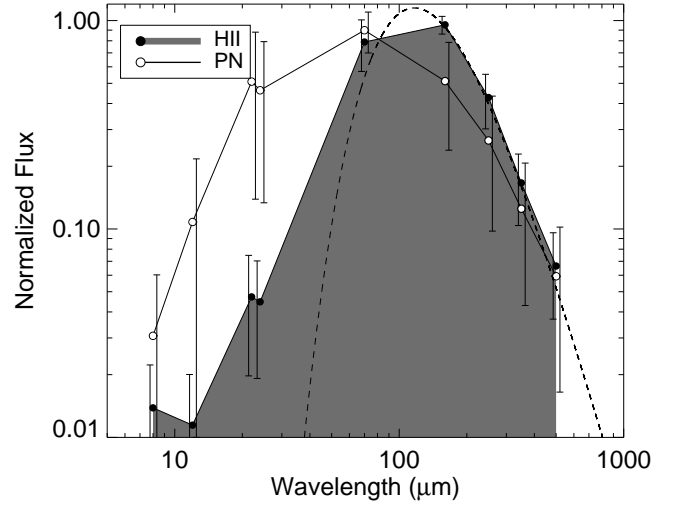


Fig. 7: Spectral Energy Distributions. Shown are the average normalized spectral energy distributions for H II regions (dark grey filled area) and PNe (black curve). The SED for dust of temperature 24.8 K is overplotted with a dashed line. Error bars show the standard deviation in each data point, and are to the left of the points for H II regions and to the right for PNe. There is considerable difference between the two average SEDs of H II regions and PNe.

PAHs). The average PN SED rises steeply from 8.0 μ m to 24 μ m, has a broad peak near 70 μ m, and decreases from 70 μ m long-ward. We find that a single temperature cannot fit the broad average SED of PNe, indicating that there is dust at a range of temperatures. The average SED for PNe looks similar to what is expected based on the SEDs of individual PNe in Hora et al. (2008) from 8.0 μ m to 70 μ m. There is, however, considerably less scatter in our 70 μ m data point than would be expected from their data. Additionally, many of their sources have higher 24 μ m fluxes than 70 μ m fluxes.

The 12 μ m WISE flux for H II regions is on average less than the 8.0 μ m GLIMPSE flux. The average ratio F_{12}/F_8 is 0.84 ± 0.26 . We do not believe this is a systematic error in the WISE 12 μ m fluxes because no such trend was found when comparing WISE fluxes with IRAS fluxes (see Figure 6), but rather is caused by the PAH emission in the 8.0 μ m band (see also §5.4).

We find that the “cold” component of the mean H II region SED is well-fit by a single temperature grey body model with a dust temperature 24.8 ± 0.2 K, when the spectral index of the dust emissivity, β , is held fixed to a value of 2.0. In these fits, we have assumed 25% of the emission at 70 μ m is due to a hotter dust component. Relaxing the assumption at 70 μ m changes the derived temperatures to 26.3 K, although the fit quality is significantly worse. The mean H II region SED shown in Figure 7 is very similar to the average SED for “bubble” H II regions shown in Anderson (2011), as are the derived dust temperature values.

Over two-thirds (68%) of H II regions in our sample peak at 160 μ m, while one third (32%) peak at 70 μ m. Of the PNe SEDs, 67% peak at 70 μ m, 23% peak at either 22 μ m or 24 μ m, and 9% (two sources) peak at 160 μ m. The two PNe that peak at 160 μ m are PNG002.2+00.5 and PNG358.6+00.7.

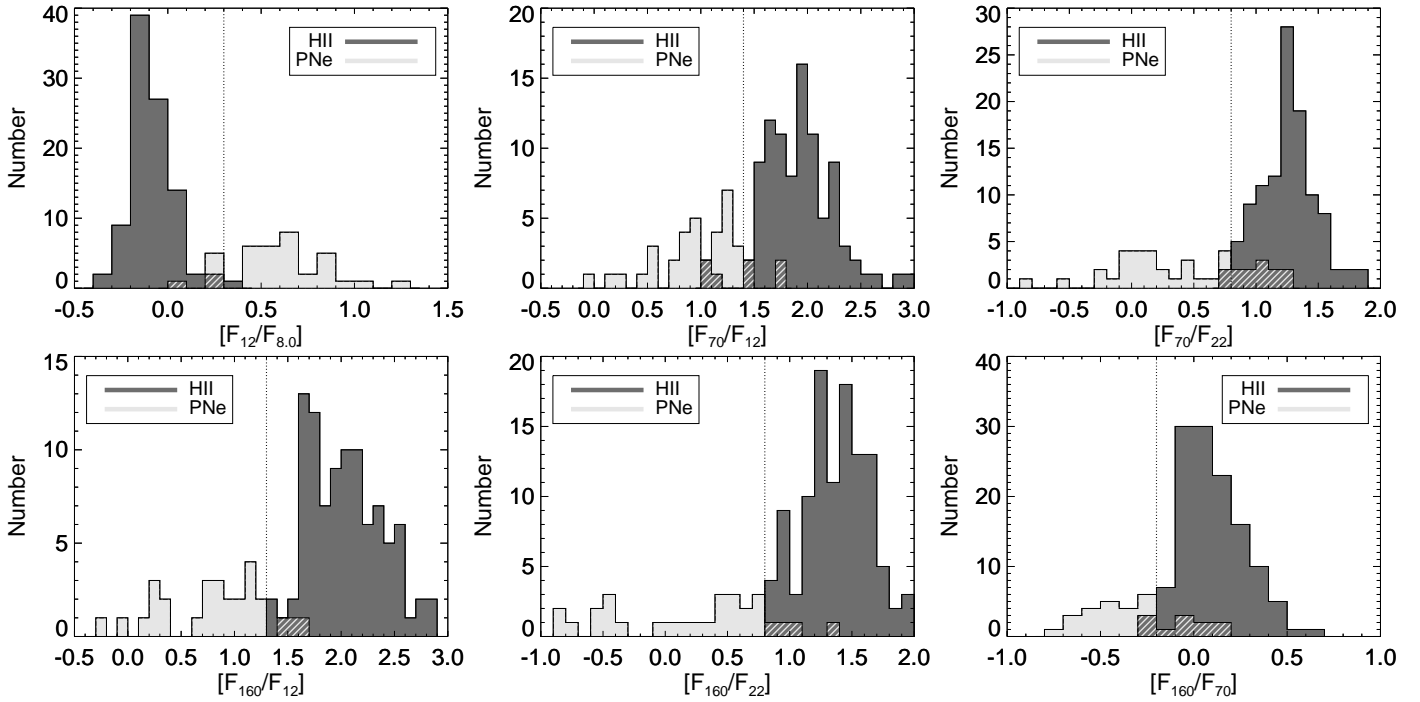


Fig. 8: IR color distributions for H II regions and PNe. Shown are the six colors (the log of the flux ratio) best able to discriminate between H II regions (dark grey) and PNe (light grey). The hatched areas contain contributions from both H II regions and PNe. The vertical dotted lines show our proposed cutoff value for separating the two populations.

Table 4: IR colors for distinguishing H II regions from PNe.

Color	Cutoff	%HII	%PNe	Avg. (HII)	Avg. (PNe)	#HII	#PNe
$[F_{12}/F_8]$	< 0.3	98	18	-0.09 ± 0.11	0.57 ± 0.29	96	38
$[F_{22}/F_8]$	< 1.0	92	20	0.59 ± 0.31	1.23 ± 0.34	110	39
$[F_{24}/F_8]$	< 1.0	93	21	0.55 ± 0.29	1.23 ± 0.31	86	37
$[F_{70}/F_{12}]$	> 1.3	96	20	1.92 ± 0.36	1.01 ± 0.40	96	40
$[F_{70}/F_{22}]$	> 0.8	98	26	1.25 ± 0.22	0.39 ± 0.51	110	42
$[F_{70}/F_{24}]$	> 0.8	100	26	1.26 ± 0.21	0.42 ± 0.47	86	41
$[F_{160}/F_{12}]$	> 1.3	100	10	2.06 ± 0.38	0.80 ± 0.49	96	30
$[F_{160}/F_{22}]$	> 0.8	100	12	1.38 ± 0.26	0.16 ± 0.64	110	31
$[F_{160}/F_{24}]$	> 0.8	100	10	1.40 ± 0.25	0.22 ± 0.55	86	29
$[F_{160}/F_{70}]$	> -0.2	97	25	0.10 ± 0.17	-0.32 ± 0.24	126	31

5.4. Discriminating Colors

We examined the distributions of all possible colors to search for the most robust criteria for discriminating between H II regions and PNe. The distributions for the most robust colors are shown in Figure 8. There, the hatched areas contain contributions from both H II regions and PNe. The vertical dotted lines in Figure 8 are our proposed discriminating color values. Throughout, we use the notation such that flux ratios enclosed in square brackets represent the log of the flux ratio.

In Table 4, we list statistics on the colors shown in Figure 8, as well the statistics of some additional colors. In Figure 8, we show colors using the WISE 22μ data in lieu of the MIPS GAL 24μ data, but we list statistics on colors found using both data sets in Table 4. Table 4 gives the color, the proposed discriminating color cutoff value, the percentage of H II regions and PNe satisfying this color cutoff, the average value of this color for the H II regions and PNe in our sample, together with their standard deviations, and the number of H II regions and

PNe that were used in the calculations. Table 4 shows that there are many different colors that can robustly separate PNe and H II regions. The three most effective colors are $[F_{12}/F_8] < 0.3$, which is satisfied by 98% of H II regions and 7% of PNe, $[F_{160}/F_{12}] > 1.3$, which is satisfied by 100% of H II regions and 10% of PNe, and $[F_{160}/F_{24}] > 0.8$, which is also satisfied by 100% of H II regions and 10% of PNe ($[F_{160}/F_{22}] > 0.8$ is satisfied by 100% of H II regions and 12% of PNe).

Table 4 shows that H II regions possess a relatively narrow range of colors. Since our sample has H II regions in a range of evolutionary states, any evolutionary effects in these colors must be relatively modest. The colors of PNe span a broader range of values compared to those of H II regions, for all colors shown in Table 4.

Most of the variation in PNe colors is real and not the result of photometric uncertainties. For example, the standard deviation in $[F_{160}/F_{24}]$ is 0.55 dex for PNe. Restricting the calculation to the 20 PNe with the highest 160μ flux for which the photometric uncertainty is relatively low, the standard deviation is 0.50; it is 0.52 for the 10 brightest

PNe. Similarly, the $[F_{70}/F_{24}]$ color has a standard deviation of 0.47 for PNe; this standard deviation is 0.43 and 0.38 for the 20 and 10 brightest PNe at $70\ \mu\text{m}$, respectively.

The colors that we have found most useful for discriminating between H II regions and PNe can be divided into three categories. First, many useful colors compare the flux at $70\ \mu\text{m}$ or $160\ \mu\text{m}$ with the flux in the MIR at $12\ \mu\text{m}$, $22\ \mu\text{m}$, or $24\ \mu\text{m}$. A simple interpretation of these colors is that they compare the emission from cold dust to that of a warmer dust component. Figure 7 shows that the average PN SED has significantly more emission in the MIR. This suggests that, relative to the cold dust component, PNe have more emission from warm dust than do H II regions. The second category are the colors comparing $12\ \mu\text{m}$, $22\ \mu\text{m}$, or $24\ \mu\text{m}$ fluxes with $8\ \mu\text{m}$ fluxes. This ratio is sensitive to the emission from PAHs, which emit strongly at $8.0\ \mu\text{m}$, and less strongly in the other bands. As stated earlier, PAHs emit much more strongly for H II regions than for PNe. Finally, the ratio $[F_{160}/F_{70}]$ is sensitive to the location of the SED peak. Since on average the SEDs of H II regions peak at longer wavelengths than PNe, this ratio will be positive for most H II regions and negative for most PNe.

5.5. Color-color Diagrams

There are numerous color combinations where H II regions and PNe are strongly segregated; the utility of an individual color-color plot depends on the available measurements and their accuracy. We show in Figure 9 color-color diagrams for two of the most robust discriminating colors. The left panel of Figure 9 shows the colors $[F_{12}/F_8]$ versus $[F_{160}/F_{22}]$ while the right panel shows $[F_{70}/F_{22}]$ versus $[F_{160}/F_{12}]$. The black dashed lines in each panel enclose 100% of our sample H II regions. In the left panel, the area enclosed by these dashed lines includes no PNe while in the right panel, only two PNe are within the area. The combination of two colors therefore shows a modest improvement in discriminating power compared to the single colors alone.

6. Application to Objects of Unknown Classification

There are numerous astrophysical objects that the criteria here derived can hopefully help classify. The power of these criteria is of course limited to separating H II regions from PNe, and may not be applicable if the object in question is neither an H II region nor a PN. Below, we test our derived criteria on additional samples of objects of unknown or contested classification. We also test the criteria on a sample of known PNe that are outside the coverage of Hi-GAL.

Some of the objects listed as PNe in Kwok et al. (2008) are not included in other catalogs of PNe. Most such objects appear visually similar to H II regions: they have diffuse MIR emission extended over multiple arcminutes and show poor symmetry. We perform aperture photometry from $8.0\ \mu\text{m}$ to $500\ \mu\text{m}$ as before (see §4) on seven such nebulae that fall within the Galactic zone studied here. These seven nebulae are listed in Kwok et al. (2008) as PNG298.4+00.6, PNG301.2+00.4, PNG321.0–00.7, PNG329.6–00.4, PNG332.5–00.1, PNG333.7+00.3, and PNG340.0+00.9. We find that six of these sources satisfy all the criteria listed in Table 4 for H II regions; their IR colors support their assignment as H II regions rather than

PNe. PNG321.0–00.7, however, has colors more similar to PNe. For example, its ratio $[F_{160}/F_{12}]$ is 0.65. This source is only a few arcseconds in diameter and seems likely to be a PN.

Many of the “disk and ring” sources seen in MIPS GAL that were cataloged by Mizuno et al. (2010) do not have definitive classifications. Mizuno et al. (2010) make a strong case that the catalog consists primarily of evolved stars, and therefore we would expect few H II regions. They list in their Appendix, however, two objects that based on their morphologies may be previously unclassified spiral galaxies. One of these, MGE351.2381–00.0145, shown in their Figure 12, appears visually similar to an H II region. For this object, the $24\ \mu\text{m}$ emission is surrounded by an $8.0\ \mu\text{m}$ ring. The morphology of MGE351.2381–00.0145 is similar to the H II region G034.325+0.211 detected in the HRDS⁵. The IR colors of MGE351.2381–00.0145 are consistent with it being an H II region: its ratio $[F_{12}/F_8]$ is -0.42 , and $[F_{22}/F_8]$ is -0.39 . We propose that this is an H II region, and the “spiral” geometry arises from line-of-sight effects, as it likely also does for G034.325+0.211. An additional object, named MGE031.7290+00.6993 in Mizuno et al. (2010), is also included in the HRDS as G031.727+0.698. This object also has $24\ \mu\text{m}$ emission surrounded by $8.0\ \mu\text{m}$ emission⁶. Its ratio $[F_{12}/F_8]$ is -0.58 , and $[F_{22}/F_8]$ is -0.13 , consistent with it being an H II region. Neither object is included in the Hi-GAL data range here studied⁷.

There are 14 HRDS sources that appear point-like at $8.0\ \mu\text{m}$. Based on their morphology, they are likely PNe rather than H II regions, although the line widths of their recombination line emission suggest that what was detected does not arise from PNe (see Anderson et al. 2011). None of these sources lie within the Hi-GAL range studied here. Of these 14 sources, only three satisfy $[F_{12}/F_8] > 0.3$, and eight satisfy $[F_{22}/F_8] > 1.0$, the colors associated with PNe. Based on these colors, some of these sources may in fact be H II regions. Without Hi-GAL data, however, our discriminating power is more limited (see Table 4).

Finally, there are a number of PNe near the Galactic Center region that have *Spitzer* data but, because of their Galactic latitudes, do not have Hi-GAL data. We analyze 11 such objects, using only GLIMPSE, MIPS GAL, and WISE data. We find that of these 11, seven satisfy $[F_{12}/F_8] > 0.3$ and $[F_{22}/F_8] > 1.0$, consistent with the colors derived for PNe.

The low success rates above show the importance of Hi-GAL data for such studies. The central white dwarf of PNe can be detected at MIR wavelengths. The contribution from the central source, relative to any contribution from a dusty shell, increases with decreasing wavelength. We hypothesize that the flux from the central source decreases the discriminatory power of IR colors at lower wavelengths.

7. Summary

Using data from *Herschel* Hi-GAL, WISE, *Spitzer* MIPS GAL, and *Spitzer* GLIMPSE, we have searched for

⁵ see http://www.cv.nrao.edu/hrds/three_color/three_color_LA229.jpg

⁶ see http://www.cv.nrao.edu/hrds/three_color/three_color_LA014.jpg

⁷ Between submission and publication we analyzed additional Hi-GAL data that were not originally available. Both sources satisfy all the criteria for H II regions in Table 4.

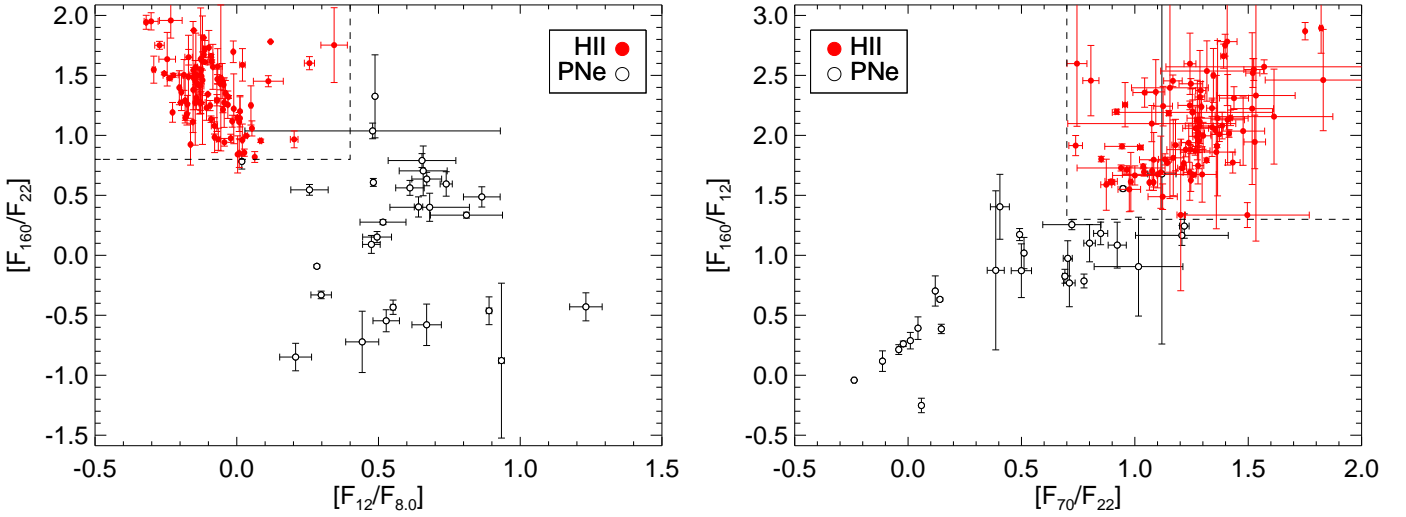


Fig. 9: Color-color diagrams for H II regions and PNe. The left panel shows the colors $[F_{12}/F_8]$ versus $[F_{160}/F_{22}]$ while the right panel shows $[F_{70}/F_{22}]$ versus $[F_{160}/F_{12}]$. The dashed lines in both panels enclose all H II regions and few PNe: none in the left panel and two in the right panel.

the most robust colors for separating a sample of 126 H II regions from a sample of 43 planetary nebulae (PNe). While our sample of PNe, which is confined to the Galactic plane and infrared bright, may not be representative of the entire Galactic population, it should be representative of PNe that may be confused with H II regions.

H II regions and PNe detected at MIR and FIR wavelengths can be reliably separated using these data, and numerous colors can be used to do so. The best color criteria are $[F_{12}/F_8] < 0.3$, which is satisfied by 98% of our sample of H II regions and 7% of our sample of PNe, $[F_{160}/F_{12}] > 1.3$, which is satisfied by 100% of our sample of H II regions and 10% of our sample of PNe, and $[F_{160}/F_{24}] > 0.8$ which is also satisfied by 100% of our sample of H II regions and 10% of our sample of PNe. Long wavelength Hi-GAL data greatly increase the discriminatory power of such IR color criteria. We applied these criteria to objects of unknown classification and were able to discriminate between H II regions and PNe in most cases. Replacing the MIPS GAL 24 μm fluxes with those of the WISE 22 μm band in the previous ratio produces a nearly identical result. The colors of H II regions span a relatively narrow range of values. Any evolution in these H II region colors with age must therefore be relatively small.

Combinations of these colors can be more effective at separating H II regions and PNe. For example the combination $[F_{12}/F_8] < 0.4$ and $[F_{160}/F_{22}] > 0.8$ includes all H II regions in our sample and no PNe.

The average SEDs of the H II regions and PNe in our sample are significantly different. The average SED of H II regions has an obvious “cold” component that peaks near 100 μm , as well as warmer component(s) that emit in the MIR and a strong contribution at 8.0 μm that may be caused by PAHs. The average SED of PNe is much broader than that of H II regions and from these data cannot be separated cleanly into temperature components. The “cold” component of the H II region SED is well-fit with a greybody of dust temperature 25 K. The SED of over two-thirds of H II regions peaks at 160 μm , while the remaining one third peak at 70 μm . The SEDs of 67% of PNe peak at

70 μm , with the remainder peaking at either 22 μm or 24 μm (23%) or 160 μm (9%).

We find that WISE 22 μm fluxes are strongly correlated with MIPS GAL 24 μm fluxes over five orders of magnitude. This suggests that the WISE preliminary release data have sufficient accuracy for the photometric measurements carried out here. The WISE 12 μm data are also well-correlated with the IRAS 12 μm data, although the scatter is larger in part due to the larger uncertainties when performing aperture photometry with IRAS data.

These results are important for future work on H II regions and PNe since the two populations can be reliably separated using photometric measurements and the discriminating IR colors derived here. These criteria will be useful when defining samples of H II regions and PNe from large-angle sky surveys.

We would like to thank the Hi-GAL team for their continuing work on the survey. PACS has been developed by a consortium of institutes led by MPE (Germany) and including UVIE (Austria); KU Leuven, CSL, IMEC (Belgium); CEA, LAM (France); MPIA (Germany); INAF-IFSI/OAA/OAP/OAT, LENS, SISSA (Italy); IAC (Spain). This development has been supported by the funding agencies BMVIT (Austria), ESA-PRODEX (Belgium), CEA/CNES (France), DLR (Germany), ASI/INAF (Italy), and CICYT/MCYT (Spain). SPIRE has been developed by a consortium of institutes led by Cardiff University (UK) and including Univ. Lethbridge (Canada); NAOC (China); CEA, LAM (France); IFSI, Univ. Padua (Italy); IAC (Spain); Stockholm Observatory (Sweden); Imperial College London, RAL, UCL-MSSL, UKATC, Univ. Sussex (UK); and Caltech, JPL, NHSC, Univ. Colorado (USA). This development has been supported by national funding agencies: CSA (Canada); NAOC (China); CEA, CNES, CNRS (France); ASI (Italy); MCINN (Spain); SNSB (Sweden); STFC (UK); and NASA (USA). This publication makes use of data products from the Wide-field Infrared Survey Explorer, which is a joint project of the University of California, Los Angeles, and the Jet Propulsion

Laboratory/California Institute of Technology, funded by the National Aeronautics and Space Administration. This research has made use of NASA's Astrophysics Data System Bibliographic Services and the SIMBAD database operated at CDS, Strasbourg, France. L.D.A. acknowledges support by the ANR Agence Nationale for the research project "PROBeS", number ANR-08-BLAN-0241.

References

- Aaquist, O. B. & Kwok, S. 1990, *A&AS*, 84, 229
- Anderson, L. D. 2011, submitted
- Anderson, L. D., Bania, T. M., Balser, D. S., & Rood, R. T. 2011, *ApJS*, 194, 32
- Anderson, L. D., Zavagno, A., Rodón, J. A., et al. 2010, *A&A*, 518, L99+
- Bania, T. M., Anderson, L. D., Balser, D. S., & Rood, R. T. 2010, *ApJ*, 718, L106
- Benjamin, R. A., Churchwell, E., Babler, B. L., et al. 2003, *PASP*, 115, 953
- Bernard-Salas, J. 2006, in *IAU Symposium*, Vol. 234, Planetary Nebulae in our Galaxy and Beyond, ed. M. J. Barlow & R. H. Méndez, 181–188
- Carey, S. J., Mizuno, D. R., Kraemer, K. E., et al. 2008, *MIPSGAL v3.0 Data Delivery Description Document* (29 August 2008)
- Carey, S. J., Noriega-Crespo, A., Mizuno, D. R., et al. 2009, *PASP*, 121, 76
- Caswell, J. L. & Haynes, R. F. 1987, *A&A*, 171, 261
- Chu, Y., Gruendl, R. A., Guerrero, M. A., et al. 2009, *AJ*, 138, 691
- Churchwell, E., Babler, B. L., Meade, M. R., et al. 2009, *PASP*, 121, 213
- Cohen, M. 2009, *AJ*, 137, 3449
- Cohen, M., Barlow, M. J., Sylvester, R. J., et al. 1999, *ApJ*, 513, L135
- Cohen, M., Green, A. J., Roberts, M. S. E., et al. 2005, *ApJ*, 627, 446
- Cohen, M., Parker, Q. A., Green, A. J., et al. 2011, *MNRAS*, 312
- Cohen, M., Parker, Q. A., Green, A. J., et al. 2007, *ApJ*, 669, 343
- Condon, J. J. & Kaplan, D. L. 1998, *ApJS*, 117, 361
- Deharveng, L., Schuller, F., Anderson, L. D., et al. 2010, *A&A*, 523, A6+
- Egan, M. P., Price, S. D., Kraemer, K. E., et al. 2003, *Air Force Research Laboratory Technical Report AFRL-VS-TR-2003-1589*
- Fazio, G. G., Hora, J. L., Allen, L. E., et al. 2004, *ApJS*, 154, 10
- García-Lario, P. & Perea Calderón, J. V. 2003, in *ESA Special Publication*, Vol. 511, Exploiting the ISO Data Archive. Infrared Astronomy in the Internet Age, ed. C. Gry, S. Peschke, J. Matagne, P. García-Lario, R. Lorente, & A. Salama, 97–+
- Griffin, M. J., Abergel, A., Abreu, A., et al. 2010, *A&A*, 518, L3+
- Hora, J. L., Cohen, M., Ellis, R. G., et al. 2008, *AJ*, 135, 726
- Hora, J. L., Latter, W. B., Allen, L. E., et al. 2004, *ApJS*, 154, 296
- Hughes, V. A. & MacLeod, G. C. 1989, *AJ*, 97, 786
- Kohoutek, L. 2001, *A&A*, 378, 843
- Kwok, S., Zhang, Y., Koning, N., Huang, H., & Churchwell, E. 2008, *ApJS*, 174, 426
- Lockman, F. J. 1989, *ApJS*, 71, 469
- Lockman, F. J., Pisano, D. J., & Howard, G. J. 1996, *ApJ*, 472, 173
- Milne, D. K. & Aller, L. H. 1975, *A&A*, 38, 183
- Miszalski, B., Parker, Q. A., Acker, A., et al. 2008, *MNRAS*, 384, 525
- Miville-Deschênes, M.-A. & Lagache, G. 2005, *ApJS*, 157, 302
- Mizuno, D. R., Kraemer, K. E., Flagey, N., et al. 2010, *AJ*, 139, 1542
- Molinari, S., Swinyard, B., Bally, J., et al. 2010, *A&A*, 518, L100+
- Parker, Q. A., Acker, A., Frew, D. J., et al. 2006, *MNRAS*, 373, 79
- Peeters, E., Hony, S., Van Kerckhoven, C., et al. 2002a, *A&A*, 390, 1089
- Peeters, E., Martín-Hernández, N. L., Damour, F., et al. 2002b, *A&A*, 381, 571
- Phillips, J. P. & Marquez-Lugo, R. A. 2011, *MNRAS*, 410, 2257
- Phillips, J. P. & Ramos-Larios, G. 2008, *MNRAS*, 391, 1527
- Poglitsch, A., Waelkens, C., Geis, N., et al. 2010, *A&A*, 518, L2+
- Pottasch, S. R., Olling, R., Bignell, C., & Zijlstra, A. A. 1988, *A&A*, 205, 248
- Price, S. D., Egan, M. P., Carey, S. J., Mizuno, D. R., & Kuchar, T. A. 2001, *AJ*, 121, 2819
- Rieke, G. H., Young, E. T., Engelbracht, C. W., et al. 2004, *ApJS*, 154, 25
- Robitaille, T. P., Meade, M. R., Babler, B. L., et al. 2008, *AJ*, 136, 2413
- Rodón, J. A., Zavagno, A., Baluteau, J., et al. 2010, *A&A*, 518, L80+
- Sewilo, M., Churchwell, E., Kurtz, S., Goss, W. M., & Hofner, P. 2004, *ApJ*, 605, 285
- Tielens, A. G. G. M. 2008, *ARA&A*, 46, 289
- Urquhart, J. S., Busfield, A. L., Hoare, M. G., et al. 2007a, *A&A*, 461, 11
- Urquhart, J. S., Busfield, A. L., Hoare, M. G., et al. 2007b, *A&A*, 474, 891
- Urquhart, J. S., Hoare, M. G., Lumsden, S. L., Oudmaijer, R. D., & Moore, T. J. T. 2008, in *Astronomical Society of the Pacific Conference Series*, Vol. 387, Massive Star Formation: Observations Confront Theory, ed. H. Beuther, H. Linz, & T. Henning, 381–+
- Volk, K. & Kwok, S. 2003, in *IAU Symposium*, Vol. 209, Planetary Nebulae: Their Evolution and Role in the Universe, ed. S. Kwok, M. Dopita, & R. Sutherland, 303–+
- Watson, C., Corn, T., Churchwell, E. B., et al. 2009, *ApJ*, 694, 546
- Watson, C., Povich, M. S., Churchwell, E. B., et al. 2008, *ApJ*, 681, 1341
- Westerhout, G. 1958, *Bull. Astron. Inst. Netherlands*, 14, 215
- Wood, D. O. S. & Churchwell, E. 1989, *ApJ*, 340, 265
- Wright, E. L., Eisenhardt, P. R. M., Mainzer, A. K., et al. 2010, *AJ*, 140, 1868
- Zhang, Y. & Kwok, S. 2009, *ApJ*, 706, 252
- Zijlstra, A. A., Pottasch, S. R., & Bignell, C. 1989, *A&AS*, 79, 329

Table 1. The fluxes of H II regions from 8.0 μm to 500 μm .

Name	ℓ deg.	b deg.	Size '	F_8 Jy	σ_8 Jy	F_{12} Jy	σ_{12} Jy	F_{22} Jy	σ_{22} Jy	F_{24} Jy	σ_{24} Jy	F_{70} Jy	σ_{70} Jy	F_{160} Jy	σ_{160} Jy	F_{250} Jy	σ_{250} Jy	F_{350} Jy	σ_{350} Jy	F_{500} Jy	σ_{500} Jy	Reference
G002.961−0.053	2.961	−0.053	1.7	4.2	0.6	2.1	0.5	6.9	0.6	8.3	1.8	460	100.0	610	29.0	600	150.0	300	71.0	100.0	22.0	HRDS
G002.611+0.135	2.611	+0.135	13.0	6.6	1.3	5.4	0.8	51.0	3.1	46.0	2.9	890	73.0	2100	110.0	830	130.0	350	66.0	110.0	23.0	Known
G002.404+0.068	2.404	+0.068	6.5	5.1	0.2	3.6	0.2	18.0	1.2	19.0	1.0	150	9.2	570	45.0	130	6.0	52	3.4	17.0	1.4	HRDS
G002.009−0.680	2.009	−0.680	1.3	2.1	0.3	1.7	0.2	7.2	0.8	7.7	0.5	130	50.0	270	61.0	130	39.0	60	14.0	22.0	4.0	HRDS
G001.488−0.199	1.488	−0.199	1.3	1.7	0.1	0.8	0.1	3.6	0.1	4.4	0.1	130	40.0	310	18.0	140	47.0	65	22.0	21.0	7.1	HRDS
G001.330+0.150	1.330	+0.150	3.2	24.0	1.4	17.0	0.7	26.0	0.3	30.0	0.3	220	49.0	900	27.0	190	66.0	84	35.0	27.0	13.0	HRDS
G000.838+0.189	0.838	+0.189	1.8	43.0	15.0	30.0	10.0	120.0	12.0	120.0	20.0	1500	640.0	3700	1500.0	1300	580.0	560	260.0	200.0	93.0	HRDS
G000.640+0.623	0.640	+0.623	3.6	170.0	32.0	370.0	120.0	140.0	10.0	170.0	21.0	4500	1100.0	8000	2000.0	3600	910.0	1500	370.0	460.0	110.0	Known
G000.382+0.017	0.382	+0.017	2.4	17.0	8.1	13.0†	6.5	84.0	8.8	65.0†	8.8	800	190.0	2400	940.0	660	140.0	260	53.0	65.0	16.0	HRDS
G359.277−0.264	359.277	−0.264	3.7	95.0	20.0	71.0†	8.1	300.0	35.0	280.0†	6.1	4300	1300.0	13000	3000.0	3200	880.0	1100	290.0	320.0	79.0	Known
G358.720+0.011	358.720	+0.011	7.1	11.0	0.8	9.6	0.4	84.0	9.8	58.0	11.0	1000	83.0	2200	330.0	960	71.0	400	27.0	120.0	7.2	HRDS
G358.633+0.062	358.633	+0.062	3.1	5.7	0.4	4.6	0.4	23.0	4.1	25.0†	5.0	400	90.0	1200	120.0	350	89.0	140	36.0	43.0	13.0	HRDS
G348.550−0.339	348.550	−0.339	2.3	0.5	0.1	0.4	0.1	4.7	0.3	5.0	0.1	82	1.0	77	5.8	31	3.8	11	1.5	4.3	0.5	RMS
G348.230−0.970	348.230	−0.970	11.9	460.0	14.0	300.0†	4.5	1200.0†	7.3	870.0†	14.0	15000	290.0	13000	980.0	4900	520.0	1700	200.0	610.0	79.0	Known
G348.225+0.459	348.225	+0.459	3.0	490.0	68.0	420.0	15.0	1100.0	14.0	1000.0	43.0	14000	1000.0	21000	4400.0	10000	2400.0	4200	880.0	1800.0	360.0	Known
G348.148+0.255	348.148	+0.255	1.4	8.9	5.0	7.6	2.5	24.0	3.1	26.0	4.4	460	82.0	910	200.0	470	93.0	180	35.0	72.0	14.0	HRDS
G347.964−0.439	347.964	−0.439	3.4	150.0	5.0	110.0	17.0	300.0	8.1	330.0	5.8	3600	92.0	5700	570.0	2900	320.0	1100	120.0	470.0	49.0	Known
G347.918−0.761	347.918	−0.761	3.5	3.1	0.1	3.2	0.1	18.0	0.4	15.0	0.5	180	2.8	130	21.0	51	17.0	19	7.6	8.3	3.3	HRDS
G347.536+0.084	347.536	+0.084	3.2	160.0	46.0	110.0	30.0	290.0	37.0	300.0	31.0	5100	530.0	5400	2200.0	2200	710.0	740	250.0	260.0	88.0	HRDS
G347.386+0.266	347.386	+0.266	10.0	2000.0	120.0	1300.0	62.0	4600.0	220.0	4400.0†	120.0	69000	2400.0	100000	17000.0	46000	10000.0	16000	3900.0	6400.0	1600.0	Known
G346.875+0.328	346.875	+0.328	2.1	4.4	1.3	4.2	0.7	8.8	2.1	10.0	2.7	230	53.0	440	81.0	220	33.0	84	12.0	35.0	4.6	HRDS
G346.539+0.097	346.539	+0.097	1.9	11.0	0.9	10.0	0.7	43.0	0.8	41.0	0.9	1000	33.0	1200	150.0	500	12.0	180	4.1	65.0	2.3	Known
G346.233−0.320	346.233	−0.320	18.5	4.3	0.8	3.0	0.6	13.0	0.4	12.0	0.8	250	15.0	300	46.0	140	25.0	54	9.4	21.0	3.6	RMS
G346.099−0.364	346.099	−0.364	2.5	13.0	3.2	10.0	1.9	13.0	1.9	14.0	3.0	260	50.0	470	160.0	210	83.0	69	15.0	30.0	13.0	HRDS
G346.077−0.056	346.077	−0.056	2.3	9.2	1.2	6.8	1.4	29.0	2.0	25.0	2.2	540	43.0	920	43.0	490	17.0	210	7.2	78.0	4.5	HRDS
G345.722+0.153	345.722	+0.153	4.1	22.0	1.0	15.0	0.5	120.0	2.7	130.0	3.3	1700	110.0	990	210.0	160	11.0	45	4.2	14.0	1.3	HRDS
G345.490+0.310	345.490	+0.310	3.7	69.0	4.9	43.0†	3.2	210.0†	5.6	180.0†	4.4	9500	110.0	11000	160.0	4800	130.0	1700	31.0	790.0	29.0	Known
G345.425−0.940	345.425	−0.940	1.4	1100.0	30.0	470.0†	8.0	2100.0†	11.0	1700.0†	11.0	51000	180.0	37000	1400.0	13000	880.0	3000	390.0	1800.0	150.0	Known
G345.215−0.749	345.215	−0.749	10.1	230.0	28.0	230.0	38.0	920.0	67.0	940.0	15.0	8400	510.0	12000	1700.0	5300	280.0	1100	150.0	920.0	40.0	Known
G345.097+0.136	345.097	+0.136	1.7	4.5	1.3	2.6	1.2	4.1	1.5	5.5	2.4	170	34.0	370	110.0	310	73.0	93	28.0	64.0	17.0	HRDS
G345.004−0.224	345.004	−0.224	2.9	2.4	0.1	1.7	0.1	73.0	0.5	31.0†	0.5	4500	6.7	5500	38.0	2100	39.0	1100	21.0	400.0	9.2	RMS
G344.439+0.048	344.439	+0.048	2.8	61.0	1.2	35.0†	1.2	190.0†	1.5	160.0†	2.4	5000	11.0	5100	83.0	2300	76.0	730	40.0	290.0	17.0	Known
G344.226−0.588	344.226	−0.588	2.4	35.0	0.8	19.0†	0.7	110.0	1.0	73.0†	0.9	3500	9.6	4800	69.0	2500	65.0	890	35.0	400.0	19.0	Known
G344.106−0.672	344.106	−0.672	1.2	26.0	2.4	15.0	3.1	58.0	2.5	62.0	1.6	1300	32.0	2500	450.0	1600	420.0	590	110.0	370.0	130.0	HRDS
G343.910+0.115	343.910	+0.115	7.3	7.3	3.8	5.4	2.7	17.0	1.0	18.0	1.9	440	49.0	730	240.0	380	200.0	170	97.0	82.0	42.0	HRDS
G343.856−0.106	343.856	−0.106	4.1	53.0	1.8	38.0	1.7	73.0	4.1	80.0	3.7	2000	68.0	2300	210.0	1100	84.0	470	15.0	200.0	5.4	HRDS
G343.721−0.221	343.721	−0.221	3.2	6.6	0.1	3.4	0.1	30.0	1.5	27.0	1.2	670	31.0	1100	130.0	590	86.0	250	37.0	100.0	16.0	HRDS
G343.490−0.033	343.490	−0.033	4.6	540.0	14.0	490.0†	14.0	2300.0†	56.0	2000.0†	63.0	21000	610.0	18000	1700.0	6800	1100.0	2300	470.0	840.0	200.0	Known
G342.061+0.420	342.061	+0.420	2.7	73.0	20.0	71.0	10.0	270.0	7.9	270.0	11.0	3200	280.0	4500	1200.0	2200	670.0	880	250.0	380.0	100.0	RMS
G340.777−1.008	340.777	−1.008	2.2	250.0	20.0	130.0†	9.4	560.0†	20.0	450.0†	13.0	14000	220.0	12000	300.0	5000	120.0	1700	49.0	620.0	23.0	Known
G340.249−0.046	340.249	−0.046	2.5	2.8	0.1	2.4	0.1	46.0	1.0	36.0	0.8	1100	21.0	1300	63.0	650	38.0	250	16.0	88.0	7.2	RMS
G340.047−0.253	340.047	−0.253	1.1	28.0	9.1	23.0†	4.9	170.0	5.8	140.0†	7.6	6400	230.0	6700	390.0	2600	170.0	1100	60.0	390.0	25.0	Known
G339.760+0.053	339.760	+0.053	1.8	5.5	0.4	3.9	0.3	8.2	0.1	9.4	0.1	170	2.8	240	19.0	110	12.0	39	5.4	15.0	2.4	RMS
G339.747+0.095	339.747	+0.095	3.2	1.2	0.2	0.6	0.1	6.7	0.5	7.5	0.5	170	6.1	380	18.0	220	15.0	88	7.6	36.0	3.9	RMS
G339.104+0.148	339.104	+0.148	7.2	10.0	1.3	10.0	0.7	60.0	0.9	45.0†	0.9	640	17.0	790	47.0	390	36.0	150	16.0	55.0	6.3	RMS
G338.681−0.084	338.681	−0.084	5.2	1.6	0.1	1.4	0.1	16.0	0.8	12.0	0.6	300	20.0	300	62.0	120	29.0	40	10.0	14.0	3.7	RMS
G338.405−0.203	338.405	−0.203	1.9	7.2	1.1	11.0	1.0	66.0	1.6	49.0†	1.6	1100	44.0	610	60.0	220	24.0	76	8.5	30.0	3.4	RMS
G338.374−0.152	338.374	−0.152	7.9	1.6	0.2	1.7	0.1	9.5	0.4	9.2	0.4	180	9.5	150	23.0	57	12.0	19	4.8	7.3	2.0	RMS
G337.995+0.077	337.995	+0.077	1.8	15.0	3.4	9.5	2.3	44.0	2.2	36.0	2.4	810	77.0	1100	170.0	570	90.0	220	34.0	89.0	13.0	RMS
G337.949−0.476	337.949	−0.476	6.1	490.0	65.0	350.0†	7.9	1800.0†	25.0	1300.0†	49.0	35000	1200.0	34000	5200.0	14000	3000.0	5500	1200.0	2200.0	490.0	Known
G337.004+0.324	337.004	+0.324	3.9	3.3	0.2	2.4	0.3	22.0	0.7	20.0	2.7	460	85.0	820	170.0	420	68.0	160	23.0	62.0	8.6	RMS
G336.773+0.246	336.773	+0.246	2.2	7.6	2.7	6.3	1.4	16.0	1.4	18.0	1.5	210	31.0	190	29.0	75	9.8	25	3.3	8.7	1.3	RMS
G335.197−0.389	335.197	−0.389	3.7	1.4	0.3	0.9	0.3	4.6	0.4	6.0	0.5	150	3.9	140	14.0	60	8.5	23	3.8	8.7	1.9	RMS

Table 1. continued.

Name	ℓ deg.	b deg.	Size '	F_8 Jy	σ_8 Jy	F_{12} Jy	σ_{12} Jy	F_{22} Jy	σ_{22} Jy	F_{24} Jy	σ_{24} Jy	F_{70} Jy	σ_{70} Jy	F_{160} Jy	σ_{160} Jy	F_{250} Jy	σ_{250} Jy	F_{350} Jy	σ_{350} Jy	F_{500} Jy	σ_{500} Jy	Reference
G334.714−0.665	334.714	−0.665	1.8	12.0	0.3	14.0	0.9	63.0	0.8	54.0	1.6	730	7.2	570	16.0	220	12.0	80	6.5	32.0	3.6	Known
G334.529+0.825	334.529	+0.825	4.6	110.0	11.0	81.0	4.8	210.0	40.0	200.0	32.0	2600	140.0	3800	490.0	1500	270.0	520	100.0	200.0	43.0	Known
G333.736−0.425	333.736	−0.425	1.5	3.3	0.5	2.9	0.3	15.0	0.8	17.0	0.7	400	19.0	410	36.0	170	22.0	64	8.3	26.0	3.1	RMS
G333.679−0.435	333.679	−0.435	9.0	4.1	0.7	3.8	0.8	18.0	3.8	17.0	3.0	320	58.0	330	39.0	130	15.0	47	7.8	18.0	4.2	RMS
G333.375−0.202	333.375	−0.202	1.6	2.7	0.4	1.8	0.2	16.0	1.1	14.0	0.6	220	22.0	320	66.0	160	35.0	61	13.0	23.0	5.1	RMS
G333.340−0.128	333.340	−0.128	1.4	3.6	1.2	3.7	0.6	33.0	1.2	34.0	1.5	290	34.0	300	53.0	160	26.0	67	12.0	25.0	6.1	RMS
G333.049+0.032	333.049	+0.032	1.3	52.0	2.9	34.0†	2.6	110.0	7.9	100.0	8.0	1800	120.0	1800	280.0	770	150.0	280	59.0	110.0	25.0	RMS
G332.978+0.792	332.978	+0.792	1.6	310.0	28.0	270.0†	15.0	1100.0†	20.0	940.0†	16.0	12000	300.0	18000	830.0	9500	460.0	3900	240.0	1600.0	110.0	Known
G332.767−0.007	332.767	−0.007	6.4	23.0	1.1	13.0	1.1	51.0	11.0	45.0	11.0	1100	190.0	1500	310.0	960	140.0	450	51.0	200.0	20.0	RMS
G332.148−0.446	332.148	−0.446	7.8	330.0	26.0	240.0†	21.0	960.0†	30.0	820.0†	15.0	13000	420.0	11000	1400.0	4000	780.0	1300	300.0	510.0	130.0	Known
G331.146+0.135	331.146	+0.135	2.6	3.3	0.3	2.6	0.2	10.0	0.7	12.0	0.9	270	31.0	530	57.0	310	21.0	140	7.0	62.0	2.9	RMS
G331.093−0.130	331.093	−0.130	3.8	1.7	0.2	1.1	0.1	17.0	1.4	14.0	1.3	190	25.0	260	42.0	130	17.0	52	6.2	20.0	2.4	RMS
G331.089+0.016	331.089	+0.016	2.0	1.6	0.1	1.2	0.1	10.0	0.3	8.4	0.3	150	26.0	300	120.0	110	17.0	43	6.5	17.0	2.6	RMS
G330.661+0.579	330.661	+0.579	1.8	4.0	0.3	2.7	0.2	6.3	1.2	6.8	1.3	140	18.0	190	81.0	97	44.0	40	17.0	17.0	6.6	RMS
G330.305−0.385	330.305	−0.385	4.3	42.0	6.6	33.0†	2.9	160.0	3.1	120.0†	4.0	3300	100.0	3400	440.0	1300	240.0	470	92.0	180.0	38.0	Known
G330.292+0.001	330.292	+0.001	2.9	0.9	0.1	0.7	0.1	6.3	0.3	5.9	0.3	93	1.7	200	19.0	120	18.0	49	9.3	20.0	4.5	RMS
G329.476+0.841	329.476	+0.841	1.3	17.0	0.5	12.0	0.4	55.0	1.0	41.0†	1.1	760	12.0	710	20.0	280	12.0	98	4.8	36.0	1.9	RMS
G329.353+0.144	329.353	+0.144	1.3	45.0	1.4	45.0†	1.0	220.0	5.6	210.0	3.2	7900	71.0	6800	120.0	2500	92.0	960	39.0	360.0	16.0	Known
G328.808+0.633	328.808	+0.633	2.2	5.5	0.1	4.3†	0.1	96.0†	2.1	45.0†	0.3	10000	14.0	6900	41.0	1700	16.0	660	5.4	290.0	2.1	RMS
G328.593−0.518	328.593	−0.518	6.7	510.0	20.0	280.0†	11.0	1100.0†	10.0	870.0†	13.0	23000	290.0	18000	1500.0	6000	940.0	2100	380.0	750.0	160.0	Known
G328.310+0.448	328.310	+0.448	3.5	190.0	5.9	160.0†	3.4	780.0†	2.6	680.0†	3.5	16000	120.0	14000	400.0	5300	260.0	1900	100.0	700.0	41.0	Known
G328.228−0.271	328.228	−0.271	9.8	0.4	0.1	0.5	0.1	7.2	0.3	5.9	0.3	46	4.1	130	22.0	85	13.0	38	5.1	16.0	2.2	RMS
G328.164+0.587	328.164	+0.587	2.5	0.6	0.1	1.0	0.1	12.0	0.4	8.9	0.5	290	12.0	480	32.0	260	19.0	100	7.4	40.0	2.9	RMS
G327.848+0.018	327.848	+0.018	1.8	1.9	0.1	1.6	0.1	8.7	0.2	8.0	0.8	150	13.0	120	5.4	43	5.0	15	2.4	4.5	1.2	RMS
G327.356−0.101	327.356	−0.101	1.3	3.6	1.2	2.9	0.7	5.5	0.7	6.6	0.8	190	17.0	250	32.0	110	14.0	40	5.1	14.0	2.1	RMS
G327.313−0.536	327.313	−0.536	1.6	1300.0	55.0	680.0†	27.0	2300.0†	120.0	1900.0†	130.0	77000	1900.0	64000	4400.0	21000	2500.0	7900	980.0	3000.0	400.0	Known
G326.448−0.748	326.448	−0.748	1.8	2.9	0.1	2.2	0.1	16.0	0.5	16.0	0.3	520	6.2	740	13.0	380	6.7	150	3.1	56.0	1.9	RMS
G326.441+0.914	326.441	+0.914	8.1	280.0	5.8	170.0†	4.5	670.0†	10.0	520.0†	9.3	12000	48.0	11000	140.0	4300	63.0	1600	30.0	620.0	16.0	Known
G325.516+0.415	325.516	+0.415	3.0	1.6	0.1	1.2	0.1	13.0	0.1	9.8	0.1	120	2.7	220	21.0	170	17.0	86	7.8	38.0	3.3	RMS
G324.192+0.109	324.192	+0.109	1.1	39.0	1.1	30.0†	1.1	170.0	5.6	140.0†	3.8	7000	51.0	6500	70.0	2500	40.0	900	17.0	340.0	7.4	Known
G323.741−0.255	323.741	−0.255	1.3	45.0	1.6	36.0	0.7	130.0	1.0	100.0†	1.4	3000	13.0	2900	34.0	1300	20.0	560	8.8	230.0	4.2	RMS
G322.407+0.221	322.407	+0.221	2.6	26.0	0.9	26.0	1.0	76.0	4.6	80.0	4.2	910	52.0	1100	83.0	420	44.0	140	17.0	56.0	6.7	Known
G322.153+0.613	322.153	+0.613	10.8	380.0	11.0	240.0†	9.1	740.0†	80.0	590.0†	75.0	23000	480.0	25000	490.0	9600	160.0	3700	55.0	1400.0	22.0	Known
G320.331−0.307	320.331	−0.307	1.7	12.0	1.1	7.8	0.9	40.0	2.0	32.0	1.5	760	26.0	750	37.0	300	36.0	100	17.0	36.0	7.2	RMS
G320.236+0.417	320.236	+0.417	1.3	210.0	4.4	160.0	3.7	330.0	4.0	330.0	2.1	6200	200.0	8700	970.0	3200	190.0	1200	78.0	500.0	31.0	Known
G320.202+0.861	320.202	+0.861	1.7	29.0	1.0	17.0	0.7	65.0	1.7	45.0†	1.0	1100	32.0	1000	96.0	420	74.0	160	34.0	65.0	15.0	RMS
G320.153+0.780	320.153	+0.780	1.6	260.0	16.0	240.0†	8.8	790.0	9.0	740.0	9.4	8800	200.0	9800	350.0	4000	140.0	1500	59.0	580.0	25.0	Known
G319.874+0.770	319.874	+0.770	1.8	170.0	15.0	130.0	9.2	260.0	14.0	270.0	13.0	4600	260.0	5300	690.0	2200	350.0	850	140.0	350.0	59.0	Known
G318.914−0.164	318.914	−0.164	2.0	16.0	2.8	15.0†	2.2	100.0	2.2	72.0†	2.1	2200	34.0	2000	110.0	820	72.0	290	38.0	110.0	21.0	RMS
G318.725−0.223	318.725	−0.223	1.5	5.2	0.1	3.7	0.1	14.0	0.1	15.0	0.1	330	3.3	410	11.0	170	8.2	62	4.5	23.0	2.7	RMS
G318.050+0.086	318.050	+0.086	2.7	2.1	0.1	2.7	0.1	33.0	0.1	28.0	0.1	1900	3.8	2000	8.7	860	9.9	310	6.0	100.0	3.2	RMS
G317.889−0.058	317.889	−0.058	1.3	5.9	1.3	5.2	0.7	24.0	0.4	21.0	0.7	550	65.0	720	310.0	230	20.0	86	8.7	35.0	3.9	RMS
G317.748+0.011	317.748	+0.011	3.6	3.0	0.5	2.3	0.5	6.1	0.6	7.1	0.7	180	6.1	250	24.0	120	19.0	48	10.0	20.0	5.2	RMS
G316.156−0.492	316.156	−0.492	6.2	34.0	1.2	20.0†	0.2	110.0	0.7	72.0†	2.1	2400	16.0	2400	62.0	1100	35.0	410	14.0	160.0	5.6	Known
G315.312−0.273	315.312	−0.273	7.6	12.0	1.2	9.4	0.6	23.0	1.2	24.0	1.2	540	13.0	950	93.0	480	70.0	210	32.0	95.0	15.0	Known
G313.458+0.191	313.458	+0.191	2.3	15.0	0.4	14.0	0.5	85.0	2.1	71.0	3.3	1600	40.0	1800	29.0	740	13.0	270	6.3	110.0	2.8	RMS
G313.446+0.176	313.446	+0.176	4.3	20.0	3.8	18.0	1.5	84.0	4.5	66.0	6.7	1600	120.0	1900	250.0	820	120.0	320	47.0	130.0	20.0	Known
G312.953−0.449	312.953	−0.449	4.0	65.0	9.2	44.0	2.8	73.0	6.2	74.0	6.3	1300	180.0	3300	150.0	1700	76.0	640	50.0	270.0	28.0	Known
G312.548−0.281	312.548	−0.281	5.1	1.9	0.3	1.3	0.1	9.3	0.1	8.5	0.1	180	4.0	300	27.0	160	17.0	66	7.3	25.0	3.1	RMS
G312.383−0.415	312.383	−0.415	2.2	4.0	0.2	2.7	0.2	23.0	0.7	21.0	0.7	320	7.1	410	36.0	240	26.0	100	12.0	45.0	5.3	RMS
G312.112+0.314	312.112	+0.314	3.0	33.0	1.7	20.0†	1.3	120.0	1.5	92.0†	1.9	2900	28.0	2900	73.0	1300	36.0	510	15.0	200.0	6.8	Known
G311.627+0.270	311.627	+0.270	2.2	20.0	1.7	21.0	12.0	110.0	15.0	71.0	2.8	3900	59.0	4400	190.0	2000	120.0	770	55.0	300.0	26.0	Known
G311.426+0.596	311.426	+0.596	4.2	14.0	0.2	8.9	0.2	30.0	0.4	26.0	0.6	540	11.0	420	13.0	140	12.0	45	5.8	15.0	2.7	RMS
G310.994+0.389	310.994	+0.389	15.3	240.0	9.0	320.0	160.0	240.0	17.0	210.0	47.0	3900	210.0	6800	260.0	2900	280.0	1100	140.0	440.0	66.0	Known

Table 1. continued.

Name	ℓ deg.	b deg.	Size '	F_8 Jy	σ_8 Jy	F_{12} Jy	σ_{12} Jy	F_{22} Jy	σ_{22} Jy	F_{24} Jy	σ_{24} Jy	F_{70} Jy	σ_{70} Jy	F_{160} Jy	σ_{160} Jy	F_{250} Jy	σ_{250} Jy	F_{350} Jy	σ_{350} Jy	F_{500} Jy	σ_{500} Jy	Reference
G310.142+0.758	310.142	+0.758	7.8	2.7	0.1	2.1	0.2	25.0	0.1	21.0	0.2	1600	3.8	1600	7.3	690	6.2	250	3.2	81.0	1.4	RMS
G309.921+0.479	309.921	+0.479	3.1	23.0	0.7	13.0	0.4	140.0	7.7	140.0†	7.3	4500	130.0	4400	290.0	1900	140.0	730	54.0	290.0	23.0	RMS
G309.548−0.737	309.548	−0.737	4.4	56.0	3.1	60.0	12.0	210.0	14.0	230.0	1.1	2000	30.0	2100	150.0	890	96.0	350	41.0	150.0	18.0	Known
G309.177−0.028	309.177	−0.028	1.9	7.8	0.5	6.6	0.5	26.0	0.6	25.0	0.5	450	2.4	510	29.0	250	21.0	100	9.0	40.0	3.6	RMS
G308.918+0.122	308.918	+0.122	3.7	74.0	1.5	47.0†	0.5	130.0	1.7	130.0†	1.3	3400	14.0	2900	61.0	1100	36.0	380	14.0	140.0	6.6	RMS
G308.647+0.579	308.647	+0.579	2.4	730.0	40.0	660.0	31.0	3100.0	67.0	3100.0	59.0	24000	910.0	27000	1500.0	10000	610.0	3700	210.0	1500.0	92.0	Known
G308.201−1.020	308.201	−1.020	1.9	1.7	0.2	1.8	0.1	16.0	0.2	12.0	0.1	110	1.5	110	5.7	59	4.2	24	1.9	10.0	1.0	RMS
G307.736−0.594	307.736	−0.594	2.8	0.6	0.1	0.6	0.1	17.0	4.3	14.0	6.4	97	18.0	240	98.0	140	55.0	66	25.0	30.0	11.0	RMS
G307.620−0.320	307.620	−0.320	25.9	260.0	34.0	260.0	16.0	1400.0	15.0	1400.0	24.0	11000	420.0	10000	2000.0	3600	1300.0	1200	550.0	490.0	240.0	Known
G307.614−0.256	307.614	−0.256	8.6	77.0	1.6	65.0	4.5	310.0	47.0	250.0†	53.0	3100	160.0	3000	63.0	1200	37.0	440	18.0	170.0	8.2	RMS
G307.561−0.587	307.561	−0.587	3.4	20.0	2.7	15.0	0.4	98.0	1.4	54.0†	2.4	1900	24.0	2500	170.0	1300	130.0	530	63.0	220.0	29.0	RMS
G306.315−0.361	306.315	−0.361	9.4	19.0	0.6	21.0	1.0	93.0	0.7	100.0	0.6	1000	6.2	1100	71.0	450	66.0	170	35.0	72.0	18.0	Known
G305.603−0.690	305.603	−0.690	3.2	1.6	0.3	1.4	0.1	12.0	0.1	9.1	0.2	67	3.2	110	12.0	76	7.1	37	3.3	16.0	1.6	RMS
G303.115−0.947	303.115	−0.947	13.2	9.9	0.7	11.0	0.6	72.0	0.6	41.0†	12.0	560	22.0	470	30.0	180	15.0	64	6.1	26.0	2.6	Known
G302.690+0.190	302.690	+0.190	7.4	120.0	13.0	90.0	6.3	300.0	5.2	300.0	8.9	4000	180.0	5700	550.0	2200	240.0	780	86.0	310.0	36.0	Known
G302.152−0.949	302.152	−0.949	1.2	5.8	0.4	5.5	0.3	32.0	0.5	26.0	0.7	350	4.2	300	15.0	130	7.5	49	3.0	20.0	1.3	RMS
G302.025−0.044	302.025	−0.044	2.3	14.0	1.8	11.0	1.0	97.0	1.1	52.0†	1.2	1700	13.0	1700	78.0	750	51.0	270	23.0	100.0	10.0	Known
G298.228−0.331	298.228	−0.331	2.7	340.0	15.0	300.0†	16.0	1500.0†	80.0	1300.0†	45.0	23000	760.0	14000	900.0	4300	250.0	2100	120.0	540.0	31.0	Known
G298.187−0.782	298.187	−0.782	6.3	46.0	1.0	36.0†	0.5	150.0	2.3	120.0†	1.7	3000	21.0	2200	26.0	760	21.0	370	14.0	97.0	4.7	Known

References. (HRDS) Anderson et al. (2011); (Known) H II regions known prior to the HRDS described in Anderson et al. (2011); (RMS) Urquhart et al. (2008).

Table 2. The fluxes of PNe from 8.0 μm to 500 μm .

Gal. Name	Name	ℓ deg.	b deg.	Size "	F_8 Jy	σ_8 Jy	F_{12} Jy	σ_{12} Jy	F_{22} Jy	σ_{22} Jy	F_{24} Jy	σ_{24} Jy	F_{70} Jy	σ_{70} Jy	F_{160} Jy	σ_{160} Jy	F_{250} Jy	σ_{250} Jy	F_{350} Jy	σ_{350} Jy	F_{500} Jy	σ_{500} Jy	Reference
PNG002.2+00.5	Terz N 2337	2.251	+0.552	27	0.190	0.015	0.570	0.038	2.10	0.12	2.30	0.63	6.50	0.42	8.40	0.93	2.70	1.30	1.60	0.53	0.77	0.31	ESO
PNG001.8−00.5	JaSt 81	1.868	−0.534	32	0.089	0.005	0.270	0.031	1.60	0.09	1.80	0.49	3.90	0.59	2.00	1.70	1.20	0.38	ESO
PNG001.6+00.1	JaSt 63	1.650	+0.188	12	0.06	0.02	0.97	1.50	ESO
PNG001.6+00.9	JaSt 55	1.635	+0.997	18	0.023	0.001	0.150	0.029	0.41	0.02	0.46	0.12	2.50	0.12	0.89	0.11	ESO
PNG001.5−00.7	K 6−17	1.509	−0.766	36	0.250	0.015	0.690	0.130	5.90	0.17	5.10	1.40	5.40	1.10	1.10	0.43	ESO
PNG001.2+00.7	JaSt 56	1.235	+0.712	18	0.011	0.002	0.071	0.010	0.37	0.09	0.35	0.10	0.63	0.41	ESO
PNG001.1+00.8	JaSt 54	1.138	+0.808	30	1.200	0.030	1.300	0.120	7.60	0.17	7.90	2.10	67.00	0.98	46.00	4.80	22.00	1.30	7.20	1.80	3.50	0.45	ESO
PNG000.8−00.6	JaSt 71	0.869	−0.696	13	0.052	0.004	0.400	0.034	2.90	0.21	2.70	0.73	3.20	0.21	0.99	0.32	ESO
PNG000.7−00.8	JaSt 74	0.748	−0.869	17	0.014	0.003	0.150	0.028	0.66	0.03	0.72	0.20	0.82	0.19	ESO
PNG000.6−01.0	JaSt 77	0.625	−1.046	32	0.150	0.004	1.000	0.035	5.70	0.08	4.90	1.30	0.84	0.17	ESO
PNG000.1−01.0	JaSt 69	0.187	−1.047	16	0.011	0.001	0.042	0.007	0.07	0.04	0.09	0.03	0.11	0.16	ESO
PNG359.3−00.9	Hb 5	359.355	−0.984	43	5.900	0.027	2.400	0.083	44.00	6.50	26.00†	7.00	100.00	1.10	38.00	2.20	18.00	1.70	7.70	1.10	3.50	0.51	ESO
PNG358.9−00.7	M 1−26	358.960	−0.721	54	2.600	0.016	6.200	0.250	83.00	3.50	31.00†	8.50	36.00	2.70	7.90	2.70	ESO
PNG358.6−01.1	JaSt 58	358.695	−1.111	15	0.057	0.003	0.260	0.048	0.42	0.14	0.38	0.12	4.30	0.66	2.10	1.30	1.10	0.37	ESO
PNG358.6+00.7	JaSt 16	358.637	+0.756	32	0.030	0.003	0.220	0.006	1.80	0.09	2.10	0.03	4.70	0.70	5.70	1.20	ESO
PNG356.9+00.9	PpA1734−3102	356.951	+0.911	44	0.200	0.004	3.500	0.210	5.20	0.15	4.30	0.05	6.00	0.17	1.90	0.58	Mash I
PNG347.2−00.8	PHR 1714−4006	347.199	−0.869	19	0.016	0.006	0.050	0.019	0.04	0.01	0.07	0.01	0.68	0.14	0.87	0.40	0.69	0.28	0.27	0.13	Mash I
PNG345.4+00.1	IC4637	345.479	+0.140	31	0.230	0.026	0.920	0.052	13.00	0.10	13.00	0.09	7.90	0.35	ESO
PNG343.9+00.8	H 1−5	343.992	+0.836	66	0.710	0.003	3.300	0.270	25.00	0.54	19.00	0.46	25.00	0.32	6.50	2.10	2.40	1.10	1.70	0.93	0.83	0.74	ESO
PNG342.7+00.7	H 1−3	342.746	+0.752	23	0.055	0.006	0.220	0.006	0.75	0.07	0.63	0.02	6.20	0.31	2.70	0.55	1.60	0.51	0.58	0.19	0.25	0.08	ESO
PNG342.2−00.3	PM 1−119	342.226	−0.380	61	0.200	0.011	1.700	0.080	17.00	0.67	12.00	0.31	13.00	0.90	2.20	1.70	1.20	0.74	ESO
PNG339.1+00.9	PHR 1639−4516	339.099	+0.989	18	0.036	0.008	0.04	0.01	0.06	0.01	0.45	0.13	Mash I
PNG337.3+00.6	PHR 1633−4650	337.314	+0.636	20	0.100	0.006	0.310	0.310	1.30	0.12	1.50	0.11	18.00	0.56	15.00	2.20	7.10	1.50	2.60	1.30	1.10	0.69	Mash I
PNG333.9+00.6	PHR 1619−4914	333.929	+0.686	37	0.790	0.072	4.900	0.270	21.00	0.36	19.00	0.26	6.50	0.41	Mash I
PNG329.5−00.8	MPA 1605−5319	329.523	−0.796	22	0.045	0.005	0.150	0.039	0.46	0.04	0.53	0.02	2.40	0.11	0.87	0.01	0.29	0.06	0.10	0.10	Mash II
PNG328.3+00.7	PHR1552−5254	328.357	+0.766	19	0.075	0.002	0.290	0.095	0.40	0.07	0.48	0.02	5.10	0.42	Mash I
PNG322.4−00.1	Pe2−8	322.469	−0.175	51	3.700	0.063	6.000	1.700	39.00	1.40	23.00	0.28	22.00	0.18	5.50	0.94	2.00	0.38	1.00	0.11	0.60	0.16	ESO
PNG322.4−00.1a	MPA 1523−5710	322.418	−0.172	26	0.040	0.003	0.190	0.027	0.78	0.21	0.71	0.10	4.10	0.36	3.40	0.59	1.40	0.38	0.58	0.18	Mash II
PNG322.2−00.7	PM 1−90	322.207	−0.743	54	0.180	0.010	0.650	0.044	4.30	0.13	4.30	0.10	6.00	0.30	1.60	0.26	0.58	0.18	Mash II
PNG322.2−00.4	BMP 1522−5729	322.198	−0.410	36	0.100	0.009	0.440	0.048	1.70	0.08	1.70	0.08	8.40	0.18	4.20	1.10	1.60	1.70	0.68	0.17	Mash II
PNG318.9+00.6	PHR 1457−5812	318.931	+0.695	33	0.130	0.008	0.620	0.170	1.70	0.08	1.90	0.02	8.10	0.27	4.20	1.40	Mash I
PNG316.2+00.8	GLMP387	316.247	+0.884	38	0.700	0.007	2.400	0.230	15.00	0.27	11.00	0.14	14.00	0.11	4.30	0.80	ESO
PNG315.9+00.3	PHR 1437−5949	315.945	+0.331	51	0.37	0.08	0.54	0.08	0.65	0.23	Mash I
PNG315.0−00.3	Hen 2−111	315.030	−0.373	41	0.230	0.010	1.200	0.094	3.30	0.10	3.80	0.06	11.00	0.29	13.00	2.60	5.30	4.90	2.10	0.96	1.10	0.53	ESO
PNG313.3+00.3		313.355	+0.312	32	0.130	0.006	0.250	0.092	0.85	0.10	0.92	0.06	0.81	0.22	Cohen
PNG309.0+00.8	Hen 2−96	309.020	+0.890	38	0.660	0.006	1.300	0.170	12.00	0.17	7.70	0.11	16.00	0.27	5.60	0.61	2.40	0.28	1.30	0.26	0.51	0.19	ESO
PNG308.1−00.5	MPA 1337−6258	308.182	−0.585	23	0.046	0.020	0.08	0.02	0.11	0.01	1.20	0.09	0.68	0.24	Mash II
PNG306.4−00.6	Th 2−A	306.416	−0.688	27	0.260	0.009	0.500	0.014	3.10	0.15	2.80	0.02	4.10	0.10	2.50	0.53	0.86	0.47	0.38	0.17	0.23	0.07	ESO
PNG305.6−00.9	MPA 1315−6338	305.599	−0.898	34	0.030	0.003	0.092	0.017	0.48	0.07	0.58	0.06	1.50	0.08	0.69	0.31	Mash II
PNG302.3−00.5	PHR1246−6324	302.373	−0.541	28	0.140	0.006	0.250	0.075	0.88	0.07	0.89	0.01	5.60	0.28	3.10	0.51	1.20	0.34	0.50	0.11	0.23	0.07	Mash I
PNG301.1−00.4	MPA 1235−6318	301.127	−0.485	21	0.008	0.001	0.028	0.002	0.12	0.03	0.13	0.01	0.11	0.08	Mash II
PNG300.4−00.9	Hen 2−84	300.429	−0.982	36	0.031	0.001	0.140	0.030	0.34	0.02	0.36	0.01	2.40	0.06	2.10	0.28	1.10	0.30	0.74	0.07	0.43	0.15	ESO
PNG296.7−00.2	MPA1157−6226	296.771	−0.211	18	0.003	0.001	0.11	0.03	0.11	0.01	1.20	0.08	0.77	0.36	0.44	0.16	Mash II

References. “ESO” for Kohoutek (2001), “MASH I” for Parker et al. (2006), “MASH II” for Miszalski et al. (2008), and “Cohen” for Cohen et al. (2005).